Monthly Notices
of the
ROYAL ASTRONOMICAL SOCIETY

MNRAS **470,** 2517–2538 (2017)
Advance Access publication 2017 May 20

doi:10.1093/mnras/stx1244

Identifying and analysing protostellar disc fragments in smoothed particle hydrodynamics simulations

Cassandra Hall,[1,2]★ Duncan Forgan[3,4] and Ken Rice[1,5]

[1]*SUPA†, Institute for Astronomy, University of Edinburgh, Blackford Hill, Edinburgh EH9 3HJ, UK*
[2]*Department of Physics and Astronomy, University of Leicester, Leicester LE1 7RH, UK*
[3]*SUPA†, School of Physics and Astronomy, University of St Andrews, North Haugh, St Andrews KY16 9SS, UK*
[4]*St Andrews Centre for Exoplanet Science*
[5]*Centre for Exoplanet Science, University of Edinburgh, Edinburgh, UK*

Accepted 2017 May 18. Received 2017 May 16; in original form 2016 December 8

ABSTRACT

We present a new method of identifying protostellar disc fragments in a simulation based on density derivatives, and analyse our data using this and the existing CLUMPFIND method, which is based on an ordered search over all particles in gravitational potential energy. Using smoothed particle hydrodynamics, we carry out nine simulations of a 0.25 $M_\odot$ disc around a 1 $M_\odot$ star, all of which fragment to form at least two bound objects. We find that when using all particles ordered in gravitational potential space, only fragments that survive the duration of the simulation are detected. When we use the density derivative method, all fragments are detected, so the two methods are complementary, as using the two methods together allows us to identify all fragments, and to then determine those that are likely to be destroyed. We find a tentative empirical relationship between the dominant azimuthal wavenumber in the disc m and the maximum semimajor axis a fragment may achieve in a simulation, such that $a_{\rm max} \propto 1/m$. We find the fragment destruction rate to be around half that predicted from population synthesis models. This is due to fragment–fragment interactions in the early gas phase of the disc, which can cause scattering and eccentricity pumping on short time-scales, and affects the fragment's internal structure. We therefore caution that measurements of eccentricity as a function of semimajor axis may not necessarily constrain the formation mechanism of giant planets and brown dwarfs.

Key words: hydrodynamics – planets and satellites: dynamical evolution and stability – planet–disc interactions – protoplanetary discs – brown dwarfs – planetary systems.

1 INTRODUCTION

There are two distinct modes of planet formation in protostellar discs. The first, and most widely accepted, is the core accretion model (CA; Pollack et al. 1996; Hubickyj, Bodenheimer & Lissauer 2005). In this model, growth begins with dust grains of ∼1 μm that coagulate rapidly into larger particles, ultimately settling into the disc mid-plane where there is enough material for them to grow to kilometre-sized planetesimals. These planetesimals can then grow via collisions into planetary cores, and if sufficiently massive, and if the gas disc has not dissipated, will accrete a gaseous envelope, ultimately becoming a gas giant planet (Lissauer 1993; Pollack et al. 1996).

Most observational evidence favours this formation mechanism. For example, gas giant planets are preferentially found around metal-rich stars (Santos, Israelian & Mayor 2004), with an empirical relationship that quantifies the probability, $\mathcal{P}$, of gas giant planet formation as

$$\mathcal{P} = 0.03 \times 10^{2.0[\mathrm{Fe/H}]}, \quad (1)$$

where [Fe/H] is the metallicity of the host star relative to solar metallicity (Fischer & Valenti 2005). Numerical work (Cai et al. 2005) has suggested that this would not be the case if the second mode of planet formation, gravitational instability (GI), were the dominant formation mechanism of these planets, since an increase in metallicity responds to a decrease in cooling rate, resulting in weaker GI activity. This ultimately decreases the likelihood of these systems fragmenting, since weak GI corresponds to smaller stresses in the disc. On the other hand, it has also been shown that

★ E-mail: cxh@roe.ac.uk
† Scottish Universities Physics Alliance.

metallicity variation makes very little difference to the occurrence of fragmentation (Boss 2002).

In the GI scenario, gas giant planets and brown dwarfs form by direct gravitational collapse in the gaseous protostellar disc (Kuiper 1951; Cameron 1978; Boss 1997, 1998). This happens rapidly, in a relatively early phase of the disc's life when it is massive enough to be self-gravitating. The advantage of this mechanism is its rapidity; gas giants are able to form on time-scales shorter than typical disc dispersion time-scales (∼5 Myr; Haisch, Lada & Lada 2001). While CA is certainly the most widely accepted model, there are barriers to grain growth at several length scales which seem to indicate difficulty in forming planetary mass objects within the disc lifetime. The most famous of these is the so-called *metre barrier*; as grains increase in size, so do their relative velocities, which makes grain fragmentation, rather than coagulation, the most likely outcome.

A promising solution to this problem is the *pebble accretion theory* (Lambrechts & Johansen 2012; Levison, Kretke & Duncan 2015). Pebbles are grouped together due to the *streaming instability* (Youdin & Goodman 2005), whereby solid particles orbit at Keplerian velocity, but the gas is pressure supported from the host stellar radiation, causing the gas to orbit at sub-Keplerian speeds. Feeling a headwind, solids slow, losing angular momentum and migrating inwards. As more solid particles migrate inwards, they cluster together, and if the solid-to-gas ratio is sufficiently large (order unity Youdin & Goodman 2005), then the backreaction of the dust on the gas will change the local gas velocity. This, in turn, alters the local drag force, promoting the pile up of solids which may gravitationally collapse if they become sufficiently large (Youdin 2011). These groups of solid particles may begin to accrete pebbles until they form giant planet cores (Lambrechts & Johansen 2012).

At smaller scales, the *bouncing barrier* prevents coagulation of dust grains, as particles of a given size, above a certain velocity, are more likely to bounce off each other than they are to coagulate. This results in growth typically halting at around ∼1 mm in size. However, there is evidence to suggest that this could be beneficial to planetesimal formation, since the introduction of a few ∼ cm sized grains (e.g. through radial drift) can act as catalyst to grain growth, sweeping up grains, while preventing the growth of too many larger objects which would otherwise smash each other apart (Windmark et al. 2012).

It is generally accepted that disc fragmentation is very unlikely in the inner regions (<50 au) of a protostellar disc (Rafikov 2005). However, the outer regions of protostellar discs may well be susceptible to fragmentation, offering a formation mechanism for directly imaged planets such as those in the HR8799 system (Marois et al. 2008; Nero & Bjorkman 2009; Kratter, Murray-Clay & Youdin 2010). Core accretion models struggle to explain objects such as those in HR8799, with four planets orbiting at 14, 24, 34 and 68 au, with masses of ∼5 M_J (Marois et al. 2008, 2010), since there is not thought to be enough material to form such massive objects at these distances. Additionally, the growth time-scales of such objects, through core accretion, typically exceed disc lifetimes by a factor of at least ∼3, using conservative estimates (Pollack et al. 1996). GI may, perhaps, offer an explanation as to the formation mechanism of these systems.

However, it has been suggested that disc fragmentation rarely forms planetary mass objects (Rice et al. 2015), with some hydrodynamics simulations (Stamatellos & Whitworth 2009) suggesting objects formed by this mechanism quickly grow to brown dwarf masses ($M > 13\ M_{\rm Jup}$), with lower limits placed on the fragment mass of ∼3–5 M_J (Kratter et al. 2010; Forgan & Rice 2011). This is compounded by the recent possible observation, for the first time, of disc fragmentation in action (Tobin et al. 2016), which shows the birth of three protostars that are well above the upper limit of the planetary mass regime.

The recent reformulation of the GI scenario in to what is now known as 'tidal downsizing' (Boley et al. 2010; Nayakshin 2010, 2011a,b; Boley, Helled & Payne 2011) does, however, have positive implications for producing low-mass planets at low semimajor axes. The key is to consider the subsequent evolution of fragments into planetary embryos, through dust growth, radial migration and tidal disruption. Forgan & Rice (2013) combined the physical processes of tidal downsizing with semi-analytic models of disc evolution (Rice & Armitage 2009) to produce the first population synthesis model for planets formed through GI. Given the similarities between these fragments and 'first cores' (see e.g. Masunaga, Miyama & Inutsuka 1998), they were modelled as polytropic spheres, with polytropic index $n = 1.5$.

They found that ∼40 per cent of fragments that formed are ultimately tidally destroyed by the central star, and of those that survive ∼40 per cent are gas giant planets with solid cores of 5–10 Earth masses, and the rest are brown dwarfs with no solid core. They also found that low-mass embryos tend to remain at larger semimajor axes due to the tidal downsizing process. Out of over 1 million fragments, there was only one terrestrial type planet (core with no gaseous envelope). These results are inconsistent with GI being the dominant planet formation mechanism, but they are certainly consistent with GI forming brown dwarfs and gas giant planets at large radii.

Population synthesis models, by necessity, make simplifying assumptions about the physics that governs the evolution of each planetary system. In particular, interactions between forming protoplanets, and the interaction of the disc with these protoplanets, are not included in the population synthesis models of Forgan & Rice (2013) that we discuss here. In fact, at the time of writing, these effects are not included in any GI population synthesis (GIPS) models. How important these interactions are in determining the final orbital configuration of a system is something that should be carefully considered before further developments are made to such a model. Quantifying the importance of these interactions is difficult, but some headway can be made by performing smoothed particle hydrodynamics (SPH) simulations of fragmenting protostellar discs, and carefully tracking the evolution of fragments' orbital and physical properties throughout the duration of the simulation.

In this work, we analyse a suite of SPH simulations of fragmenting protostellar discs, identifying fragments using two different methods. The first, based on the `CLUMPFIND` algorithm (Williams, de Geus & Blitz 1994; Smith, Clark & Bonnell 2008), is done using the gravitational potential, and the second is a new method that uses density derivatives. We do not use sink particles (Bate, Bonnell & Price 1995) in our simulations, as by using only SPH particles, we are able to determine the fragment internal structure as it migrates through the disc, and better understand the orbital evolution of the fragment, which is sensitive to its radial mass distribution. We discuss the relative merits of our different detection methods for our simulations, which show a variety of fragmentation scenarios. We consider the implications of our results for current GIPS models, and finally we consider the orbital and physical properties of the fragments in the simulations, comparing them to the orbital and physical properties of the population synthesis models of Forgan & Rice (2013).

The paper is ordered as follows: In Section 2, we describe our overall method, outlining our chosen formalism of SPH in Section 2.1 and detailing the simulation setup in Section 2.2. We

present our algorithms in Section 2.3, describing our new approach in Section 2.3.2 and our adaptation of an existing approach in Section 2.3.1. We describe our results in Section 3, detailing the relative merits of the different approaches in Section 3.1. We compare our results to current GIPS models in Section 3.2. We outline orbital and spin properties of our fragments in Sections 3.3 and 3.4, respectively. We describe density and temperature profiles of fragments with the most interesting histories in Section 3.5, and discuss our findings and conclude in Section 4.

2 METHOD

We run a suite of nine SPH simulations, with the radiative cooling method of Forgan et al. (2009). Each disc uses 4 million particles, fragments to form at least two bound objects, and – aside from the random number seed used to initialize each disc – has identical initial conditions. Since our aim is to take advantage of running a fully hydrodynamic simulation by tracing the evolution of fragment radial profiles and mass distribution, we run the simulations for as long as it is computationally feasible using hydrodynamics only (without switching to sink particles). In practice, this means running each simulation until the most dense clump becomes too dense to calculate the next time-step. We give a brief description of SPH, and our selected radiative transfer formalism, in Section 2.1. We discuss our methods of finding fragments in Section 2.3.

2.1 Smoothed particle hydrodynamics

SPH is a Lagrangian hydrodynamics formalism that evolves a fluid by means of a distribution of pseudo-particles (Gingold & Monaghan 1977; Lucy 1977). There are many review articles about SPH (see e.g. Monaghan 1992, 2005; Rosswog 2009), but the basic idea is that each particle has a position, mass, internal energy and velocity, and these parameters can be interpolated over to give fluid quantities at any position. Density is calculated by interpolation over the mass distribution, and pressure is determined using an equation of state with internal energy. Gravitational forces are usually computed using a TREE algorithm (Barnes & Hut 1989), and then the discretized energy and momentum equations are solved. Particle velocities are updated using pressure and gravitational forces, and positions are then updated using these velocities. Internal energy changes are computed by calculating $P\mathrm{d}\,V$ work, viscous dissipation and radiative cooling and heat conduction.

Cooling calculations in SPH are no simple task. Accounting for polychromatic radiative transfer within a hydrodynamics simulation is not possible with current computational resources, and even post-processing a single snapshot with radiative transfer is computationally expensive (Stamatellos & Whitworth 2005). Historically, approximations to individual features of radiative transfer were used, such as the cooling time formalism: $\dot{u} = -u/t_{\rm cool}$ (Rice et al. 2003a). Although this parametrization is useful, allowing us to probe the effects of different cooling time-scales in protoplanetary discs, it is somewhat limited, as it only allows us to model energy lost from an SPH particle. Realistically, if energy is lost from one SPH particle, at least some of that energy will be gained by its surrounding neighbours – this is known as radiative transfer.

Since our aim here is to trace the orbital and profile evolution of fragments within protostellar discs, we wish to capture the effects of radiative transfer as far as is feasible. Therefore, the cooling we implement is the hybrid method of Forgan et al. (2009). The details of the algorithm are given in Forgan et al. (2009), however the basic ideas merge the polytropic cooling method of Stamatellos et al. (2007) with the flux-limited diffusion method of Mayer et al. (2007), which builds on conduction modelling work by Cleary & Monaghan (1999) and the flux-limiter described in Bodenheimer et al. (1990). The biggest advantage is the complementary nature of these two methods, energy loss is handled by polytropic cooling (which flux-limited diffusion cannot do), and positive energy exchange between neighbouring particles is handled by flux-limited diffusion (which polytropic cooling cannot do). Since each method handles a separate process, there is no 'double counting' in any part of the system's overall energy, and these separate parts can simply be summed to calculate the total energy change.

2.2 Simulation setup

We run a total of nine simulations of 0.25 $\mathrm{M}_\odot$ discs, with a 1 $\mathrm{M}_\odot$ central star, an inner radius of 10 au, an outer radius of 100 au and a radial density profile of $\Sigma \propto r^{-1}$. All discs are initially identical in global properties, varying only the random number seed (the integer used to set the starting point for a sequence of random numbers) used to initialize the disc. The SPH particles are randomly distributed in ϕ, where ϕ is azimuthal angle, and the r position of each particle is determined through the iterative use of an accept-reject algorithm, accepted so long as the position of the particle maintains the desired surface density profile. The z position of the particle is similarly determined, accepted so long as the position maintains hydrostatic equilibrium. The velocity of each particle is exactly Keplerian. This technique results in discs that are identical in their global properties, differing only through a small amount of noise at the particle-separation level.

All discs are evolved until it is no longer computationally feasible to continue, which in reality means the density of a fragment has become so high that time-steps cannot be computed without switching that mass to a sink particle. However, since here we wish to examine physical and orbital properties of the fragments which are influenced by their radial mass distribution, we do not do this. All of the simulations fragment to form at least two bound objects, and their ultimate configuration is shown in Fig. 1, which shows nine column density plots, in physical units, and illustrates a variety of fragmentation scenarios as the simulation's final configuration. We discuss this in detail in Section 3, but include images now to make the explanation of our methods in Section 2.3 clearer.

2.3 Algorithms

We present here two methods of detecting fragments in SPH simulations, and one method of linking them together between time-steps. Once a fragment has been identified, we then refer to it as a 'clump'. The first method of detection is based on the clump finding approach of Smith et al. (2008, which is in turn based on the publicly available `CLUMPFIND` algorithm developed by Williams et al. 1994). The basic idea is to perform an ordered search on SPH particles from high (physical) density to low density. The highest density particle i forms the centre of a clump, and if the next particle in the list is a neighbour (i.e. in close spatial proximity), it is also added to this clump. If it is not a neighbour, it forms the centre of a new clump. This process is continued to the next most dense particle, until a minimum density threshold is reached. The search in this manner, from least dense to most dense particle for our SPH simulations of protostellar discs was unsuccessful in identifying clumps in our simulation. We are faced with a different scenario to Smith et al. (2008), who used their algorithm in molecular cloud cores. Once our discs have evolved enough to fragment, the inner disc is so dense

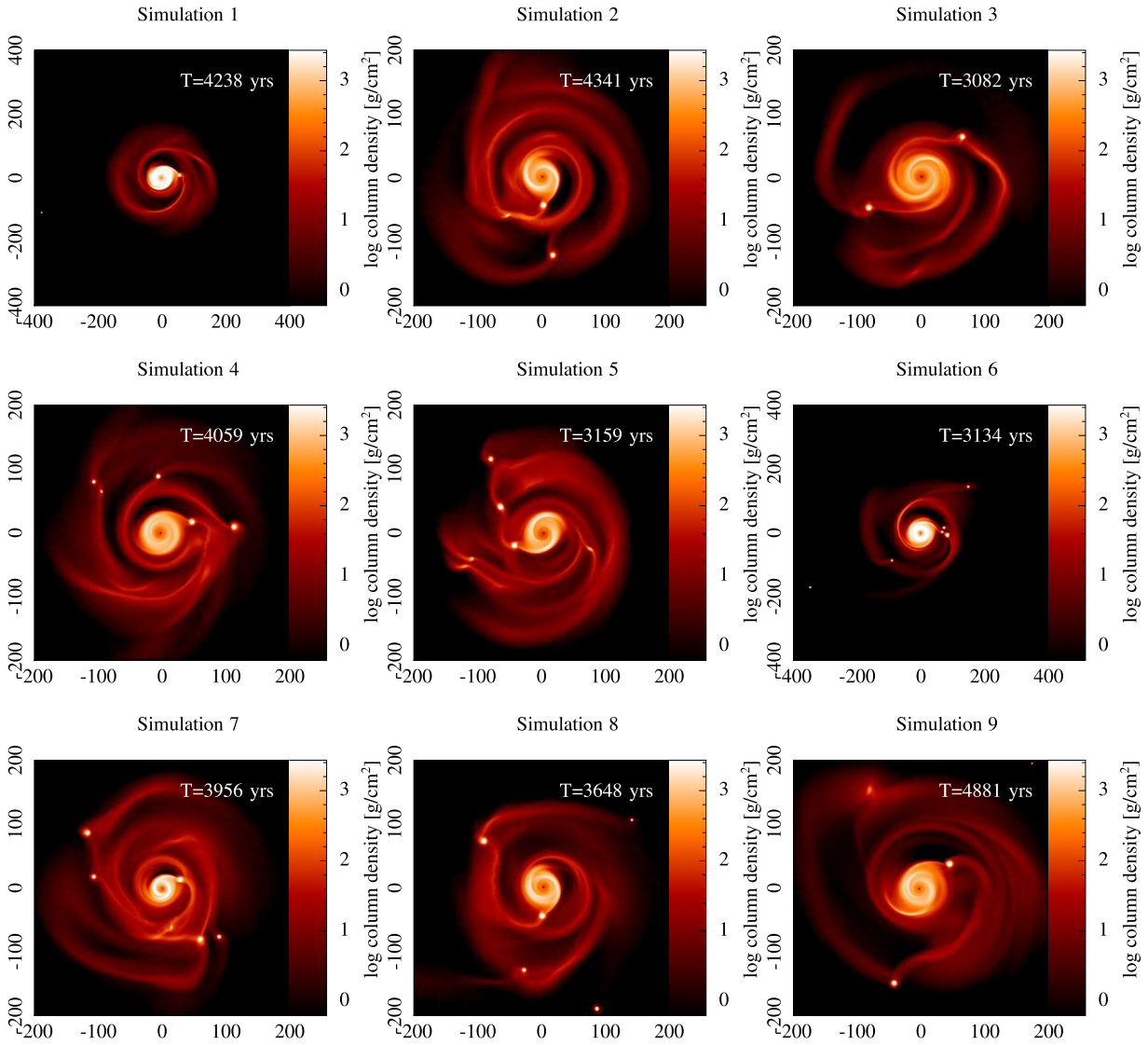

Figure 1. Column density plots of the final fragment configuration for all nine simulations. Despite almost identical initial conditions, there are a variety of ultimate configurations, and a variety of times at which it becomes computationally unfeasible to continue the simulation using only hydrodynamics. Simulations 1 and 6 show an ejected clump at large radial separation, and the top left hand corner of simulation 9 shows a fragment forming just below the threshold detection of our algorithm.

that many of the particles inside ∼20 au fulfil the criteria to become the head of their own clumps. This results in neighbours, since this is a friends-of-friends algorithm, belonging to these even if they are in the outer disc, where fragmentation has actually occurred.

This problem was solved, to some extent, by using the gravitational potential of the particles, rather than the density, for the ordered search. We discuss this method in Section 2.3.1. The inability of this method to identify low mass, fluffy fragments, or fragments that are so deep in the potential well of the central star that they are ultimately tidally destroyed, prompted the development of an approach that could correctly identify such fragments. The approach uses a gridded derivative search of the SPH interpolated density of the particles, and is discussed in Section 2.3.2.

Finally, in both cases, the clumps are linked between time-steps using a merger tree algorithm, typical of dark matter halo tracers in cosmological simulations (see e.g. Srisawat et al. 2013). This process is detailed in Section 2.3.3.

2.3.1 *Gravitational potential search (`CLUMPFIND`)*

Broadly speaking, clumps are created with a unique integer identifier (ID) at the local minima of the gravitational potential, so long as there are at least a minimum number of neighbour particles above some defined 'noise' level. For our purposes, we define this critical number as $n_{\rm critical} = n_{\rm mean} - 5n_{\sigma}$, where $n_{\rm mean}$ is the mean number of neighbours each particle has, and $n_{\rm sigma}$ is the standard deviation of the number of neighbour particles. We do this because the neighbour lists of particles at low density can be sparse due to the algorithms used to calculate the smoothing length, h.

We begin by creating a clump at the location of the central sink particle (star). All particles are then sorted by their gravitational potential energy, and we loop over the particles in order of most negative to least negative gravitational potential energy (i.e. most bound to least bound). We select the particle, i, with the most negative potential energy, and as long as it does not already belong to a clump (in which case, we exit and select the next particle), we

iterate over particle i's neighbours, j. If the majority of the neighbours j (>50 per cent) are in a clump k, the particle is also in clump k. We assign the particle ID of i to $\mathrm{ID}_i = k$ and exit. If the majority of i's neighbours are not in a clump, then since i is the most bound particle (MBP) it starts a new clump l, provided that $n_{\mathrm{neighbours}} > n_{\mathrm{critical}}$. We then loop over particle i's neighbours j, assigning $\mathrm{ID}_j = l$ so long as j is not already in a clump. We then proceed to next MBP, $i + 1$, and repeat (Forgan, Price & Bonnel 2016).

2.3.2 *Density derivative search*

In this method, we compute a 2D grid in cylindrical r and ϕ coordinates, and bin all particles into these grid cells. The maximum density of a particle in each cell is then taken to be the peak density in that cell, ρ_i, which gives us a 2D sheet describing density maxima. The number of bins required to reasonably identify all clumps varies due to the stochastic nature of the simulations, more fragments with low density at ∼100 au require a larger number of bins to properly resolve, with our resolution criterion being that the number of clumps ultimately detected by the search is equal to the number of clumps that are determined 'by-eye'. If fewer clumps are detected by the search than 'by-eye', then the resolution is increased until we detect these low-mass, low-density clumps. A typical resolution is 10 000 radial bins and 7200 azimuthal bins.

We next take the derivative of the peak density in that cell with respect to r and ϕ. As this is noisy in density space, we smooth these derivative, equivalent to making a new signal, where the element is now the average of n adjacent elements, such that

$$\frac{\partial \rho_i}{\partial r} = \frac{1}{n} \sum_{j=-\frac{n-1}{2}}^{j=\frac{n-1}{2}} \frac{\partial \rho_{i+j}}{\partial r} \tag{2}$$

and

$$\frac{\partial \rho_i}{\partial \phi} = \frac{1}{n} \sum_{j=-\frac{n-1}{2}}^{j=\frac{n-1}{2}} \frac{\partial \rho_{i+j}}{\partial \phi}. \tag{3}$$

Despite its simplicity, this approach is best at removing white noise while keeping the sharpest step response. The value of n (∼100 is typically sufficient), like the number of bins in which to bin the data, must be optimized by the user to get the best compromise between smooth data, which removes false peaks, and data which is sensitive enough to identify small clumps.

We then use this smoothed derivative to identify clumps, which will be a 'real' peak in the density. A real peak is identified by a sustained zero-crossing of the derivative with a negative gradient. Peaks due to noise will also have zero-crossings, but they are sustained for fewer bins than real peaks. These false peaks can be eliminated by requiring that the zero-crossing is sustained for m bins, with m optimized by the user to remove most (if not all) false detections while still detecting less dense clumps.

The radial search is shown in Fig. 2, which shows the radial density profile (blue solid line) and the derivative of the radial density profile (dashed red line) for the disc shown in simulation 6 of Fig. 1. The zoomed section shows the peak of a clump, with the negative gradient zero-crossing of the derivative identifying the peak.

Once the particle marking the centre of a clump (i) has been identified, we add all of i's neighbour particles j to that clump. We now loop over all particles which form that clump, adding their neighbours to this clump as well. We repeat this until we reach some density threshold. We found that adding neighbour particles

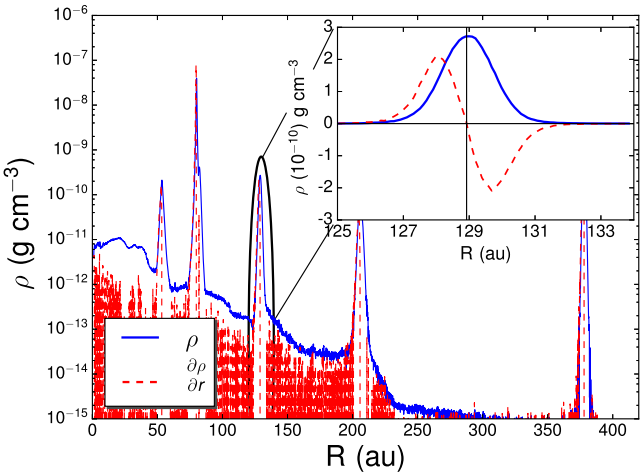

Figure 2. Our density derivative search method on the disc shown in Fig. 1, simulation 6. The solid blue line shows the radial density profile of the disc, and the dashed red line shows the derivative of this with respect to r. The zoomed region demonstrates how the negative zero-crossing of the derivative identifies one of the real density peaks.

until more than half the particles in the neighbour sphere are less dense than the inner 1 au of the disc produced good results. Once we have identified the bulk of the clump, we then proceed with a potential search described in Section 2.3.1, which determines to which clumps the rest of the unidentified particles in the simulation belong.

2.3.3 *Merger tree*

At this point, we have a set of clumps in each time-step, and we need to track them over the duration of the simulation. To do this, we use a standard algorithm from halo tracking in cosmological simulations (see e.g. Springel et al. 2001). Each clump, in each time-step, is given an integer ID by our algorithm. So that we can trace the evolution of this clump throughout the simulation, these IDs must be linked. Since we are modelling fluid through the use of pseudo-particles, the particles, that make any given clump, change between dumps, sometimes substantially. To link clumps, the crucial factors are the MBP, and shared member fraction (SMF). In our density derivative search (DDS), we actually trace the most dense particle, rather than the MBP, but we use the term interchangeably to avoid the introduction of unnecessary acronyms. To be identified as the same clump between time-steps, they must share the MBP and have an SMF of >50 per cent. In some particularly volatile simulations, when using the density derivative method, the MBP may change, and the SMF may be <50 per cent. In this case, some of the clumps need to be manually linked during post-processing by tracing a group of particles in each clump in each time-step. The basic algorithm is as follows:

(1.) Loop over clumps i in previous time-step *lastdump*.
(2.) Find clump j, in this time-step *thisdump*, which contains the MBP from clump i in *lastdump*.

(i.) If MBP_i does not belong to any clump in *thisdump*, clump i is not present in *thisdump*.
(ii.) If MBP_i belongs to clump j in *thisdump*, and clump i and j share at least 50 per cent of particles, then $\mathrm{ID}_j = \mathrm{ID}_i$, and the clumps are linked between the two time-steps.

(iii.) If MBP_i belongs to clump j in *thisdump*, but clumps i and j do not have SMF $>$ 50 per cent of particles, then clump j keeps its present ID.

(3.) End loop over previous time-step.

(4.) Loop over clumps in *thisdump*, checking for clumps with no progenitors in *lastdump*. Increment the maximum number of distinct IDs by the number of new clumps, and assign each clump the correct ID.

3 RESULTS

We ran a total of nine SPH simulations with almost identical initial conditions, differing only in the random number seed used to initialize the disc. Column density plots of the nine simulations are shown in Fig. 1. Despite the almost identical initial conditions, there is a large variation in final configurations and number of clumps in the system.

Our results sections fall into three broad categories – first, the relative merits of the two methods and the difference in clump detection between them. We show that, interestingly, our density derivative search detects all clumps that are detectable by eye, whereas our ordered potential search does not. In fact, generally speaking, the potential search does not detect any clump that is eventually destroyed, giving a good indicator of the likelihood of a clump's survival.

We next discuss the implications of our results for current population synthesis models, comparing our clump mass and semimajor axis functions to existing population synthesis models. We show the clump interaction needs to be included in GIPS models as early as during the gas phase, as scattering plays an important role.

Finally, we discuss interesting events in the simulations themselves. We introduce a piece of nomenclature now, to avoid confusion, that S*a*C*b* means simulation *a*, clump *b*. This abbreviation is given in the title of any plot of a specific clump. Note that our clump numbering begins at 2, since clump 1 is the star+disc system. We also state now, for clarity, that any mass stated for our clumps *includes* unbound material. This is deliberate, in order to track more of the mass of the clump. Furthermore, what is currently unbound material around the clump, at these very early times, may eventually lose spin angular momentum through interactions with material in the disc, ultimately becoming part of the clump. By including the unbound material, we trace more of this process from earlier times. For high-mass clumps ($>$20 M_J), the amount of unbound material is small, typically around 10 per cent or so. This is larger for lower mass clumps, up to $\sim$25 per cent of material identified may be unbound, rising to 40 per cent in clumps occurring in particularly volatile simulations that have many clumps, as their formation is often disrupted by interactions with other.

We look at the orbital properties of the clumps, and discuss clump mergers and tidal destructions by the central star. We show that: (1) destruction and merging are fairly common, (2) interactions between clumps can result in a clump changing its direction of spin from prograde rotation to retrograde rotation and (3) retro-rotating clumps typically have more dramatic changes in their radial temperature profiles than prograde clumps.

3.1 Relative merits of gravitational potential energy search and density derivative search

We identified clumps in our simulation using two different search methods, an ordered potential energy search (OPS) based on Smith et al. (2008), and a novel approach based on a 2D DDS. Our first conclusion is that searching using the ordered potential of the particles only detects clumps that survive the duration of the simulation. However, using the DDS method, destroyed clumps are also detected. This is shown in Fig. 3, which shows the total change in semimajor axis, from when the clump is first detected to when the clump is last detected (or destroyed), against the total time for which the clump exists, i.e. from initial identification to the end of the simulation, or the last time-step in which it is identified, if it is destroyed. Larger markers indicate more massive clumps. The left-hand panel shows the DDS results, the right-hand panel shows the OPS results. Circular markers indicate clumps that have survived until the end of the simulation, square markers indicate clumps that are destroyed, and triangle markers indicate a clump that merged into another clump. There are no identical markers in both plots because the different algorithms detect the clumps at different times therefore they migrate different distances.

In addition to containing no destroyed clumps, the OPS sample also has a relative insensitivity to clumps which will have a final mass of less than $\sim$5 M_J, and detects most of the clumps later in the simulation. This is shown in Fig. 4, which shows mass accretion histories for clumps in each of the nine simulations, as is detected the OPS. By comparison, Fig. 5 shows the same nine simulations, but with the mass accretion histories of the clumps determined by using the DDS method. As can be seen, many low-mass clumps evade detection entirely under the OPS method; for example, simulation 6 has an additional three clumps that are not detected by the OPS, and those that are detected are generally detected later, such as clump 2 in simulation 2, which is detected $\sim$400 yr later in the OPS than in the DDS.

This is due to the nature of the potential search. Fig. 6 shows the radial gravitational potential energy profile of the disc in Fig. 1, simulation 6. Since the OPS proceeds from the particle with the most negative gravitational energy to the most positive, the OPS detects the clump at $\sim$80 au in Fig. 6 first, and then detects the clump at $\sim$375 au second. However, it fails to detect the clumps at $\sim$50, $\sim$125 and $\sim$200 au. This is because particles at the potential energy of the main body of the disc are identified as belonging to the clumps with the most negative potential energy during the neighbour check described in Section 2.3.1. Then, when the particles belonging to clumps at 50, 125 and 200 au are checked, they are found to already belong to either the main body of the disc (i.e. the central sink) or one of the clumps with the deepest potential well.

Although this could be fixed by adopting a gridded approach to the potential search (thereby eliminating the dominating effect from the clumps with the largest potential well), OPS has a desirable feature, namely demarcating clumps that are likely to survive the simulation, and those that are not.

The OPS method's insensitivity to small clumps, and reliance on deep potential wells for identifying the body of the clump, mean that fewer clumps are detected by the OPS method, and those that are identified are often initially identified at artificially small masses ($\sim 10^{-3}$ M_J), as there is only a small amount of mass with a potential well deep enough to be identified. This can be seen in Fig. 4, which shows mass accretion histories for all nine simulations using the OPS method. In every simulation, what ultimately grows to be the largest clump is initially identified with a mass well below the Jeans mass. The DDS search method, however, does a better job of correctly identifying the mass associated with the young clumps, typically identifying between 5 and 10 M_J of mass. This is shown in Fig. 5, which shows the mass accretion histories for all nine simulations, as identified using the DDS method.

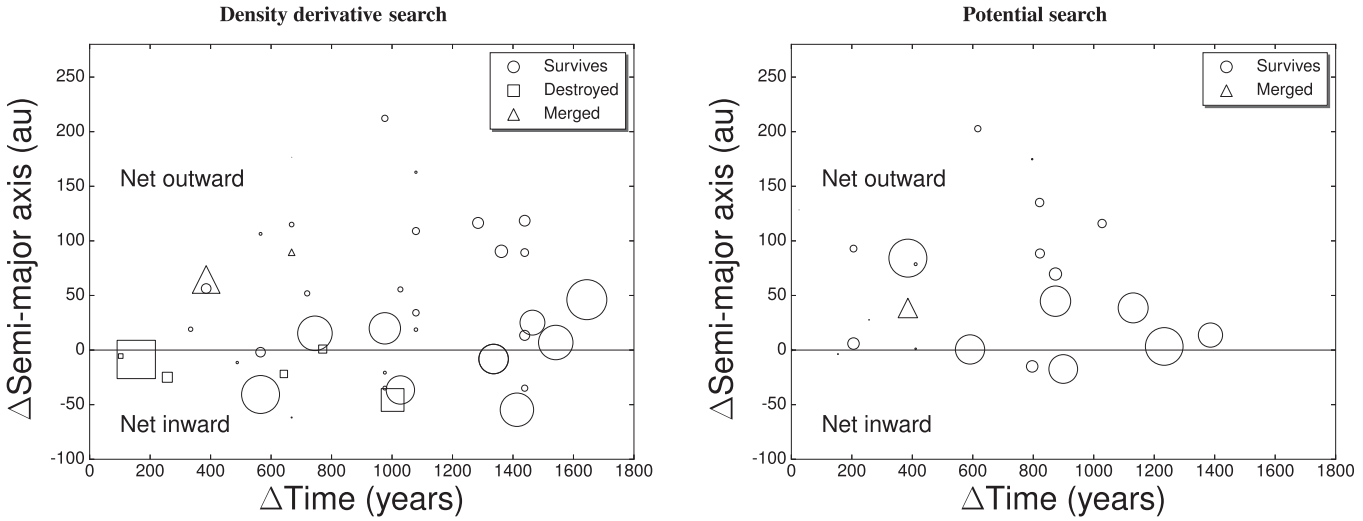

Figure 3. Plots showing total change in semimajor axis, for all clumps in all nine simulations, plotted against the time between initial identification, and the either the end of the simulation, or the last time-step in which they are identified, if they are destroyed or merged. Larger markers correspond to more massive clumps. The left-hand panel shows clumps as they are identified by our density derivative search method, and the right-hand panel shows clumps as they are identified using our ordered potential search method. Circular markers indicate the clump survived the duration of the simulation, square markers indicate tidally destroyed clumps and triangle markers indicate the clump was subsumed by another clump. The right-hand panel shows that clumps that are ultimately destroyed are not detected by the ordered potential search. The left-hand panel shows that ∼20 per cent of fragments are ultimately tidally destroyed. There are no identical markers in both plots because the clumps are detected at different times in the simulation, and thus migrate different distances.

In addition to the difference in measured initial clump mass, both methods differ in the final mass attributed to clumps. Typically, the growth is smoother for the OPS method, since once mass is deep in the potential well it is unlikely to change. However, if the gravitational potential energy profile of the disc changes then so too will the attributed mass of the clumps.

Another feature of the DDS method is its ability to identify low-mass, low-density clumps that do not have a strong signal in their potential. This can be seen in Fig. 5, simulation 6, which identifies an additional three clumps compared to Fig. 4, simulation 6. Comparing Fig. 6 and Fig. 2, we can see that these clumps have much stronger signals in their radial density profiles compared to their radial potential energy profiles. This is a useful predictive feature, since the left-hand panel of Fig. 3 and all of Fig. 5 show that ∼20 per cent of the fragments in our simulations are tidally destroyed (we discuss the implications of this for population synthesis in Section 3.2), none of which are detected in the OPS method.

Therefore, if a clump is detected in the DDS and not in the OPS, it is indicative that either the clump will stay relatively low mass and not accrete further, or that it will be tidally destroyed.

3.2 Comparison to gravitational instability population synthesis models

We ran the Forgan & Rice (2013) GIPS models for 4000 yr, which is comparable to the time-scale for which our SPH simulations are able to run until no longer computationally feasible. We dictated that the opacity power law be $p_k = 1$, and that the disc is not truncated after fragmentation. Fig. 7 shows initial and final mass and semimajor axis distributions for the GIPS model and for the clumps in our SPH simulation. The red, hatched histogram is the population synthesis, blue outline is the SPH clumps. The left-hand panel of Fig. 7 shows the initial and final semimajor axis distributions for both samples, and the right-hand panel shows initial and final mass distribution for both samples. We cut off the tail of the initial and final masses beyond >35 M$_J$, since we cannot feasibly simulate masses above this without switching to sink particles.

Comparing the initial mass and semimajor axis distributions in the GIPS models to our SPH clumps, it would initially appear that clumps in SPH simulations form much further out, and at much lower masses, than in the population synthesis models. In reality, this is somewhat a limitation of our identification algorithms, as at very early times, the clumps can escape detection because of their low density/less negative gravitational potential energy, such that they have already undergone some radial migration before they are detected. If they have undergone sufficient radial migration, they may be far enough out in the disc to not accrete much material, hence remaining low mass.

Having established that the initial mass and semimajor axis distributions for our SPH clumps are subject to some limitations of our detection algorithm, we now compare the final mass and final semimajor axis distributions of our SPH clumps to those in the GIPS model. First, the bottom left-hand panel of Fig. 7 shows a dearth of clumps at $R < 25$ au, when compared to the GIPS model – this is simply due to the last measured value of a before the fragment is destroyed. This figure also shows that the distribution of semimajor axes is different to what is expected, given the GIPS model data, and therefore the mechanism that allows these separations to exist at early times (i.e. clump–clump interactions) plays an important role in the ultimate orbital distribution function of the sample.

Second, the bottom right-hand panel of Fig. 7 shows that our final mass distribution is bimodal, with peaks at ∼5 and ∼30 M$_J$. This is somewhat consistent with previous measurements of mass distributions of fragmenting discs by Vorobyov, Zakhozhay & Dunham (2013), who find that there are two maxima in their mass distribution, at ∼5 and ∼ 60 M$_J$. Unlike Vorobyov et al. (2013), we find a gap at ∼15 M$_J$, whereas they find a minima at ∼25 M$_J$, and our second maxima is at ∼30 M$_J$ rather than ∼60 M$_J$. Given our small N statistics, we would probably expect our distribution to converge on a minima at ∼15 M$_J$, rather than the gap that is currently present.

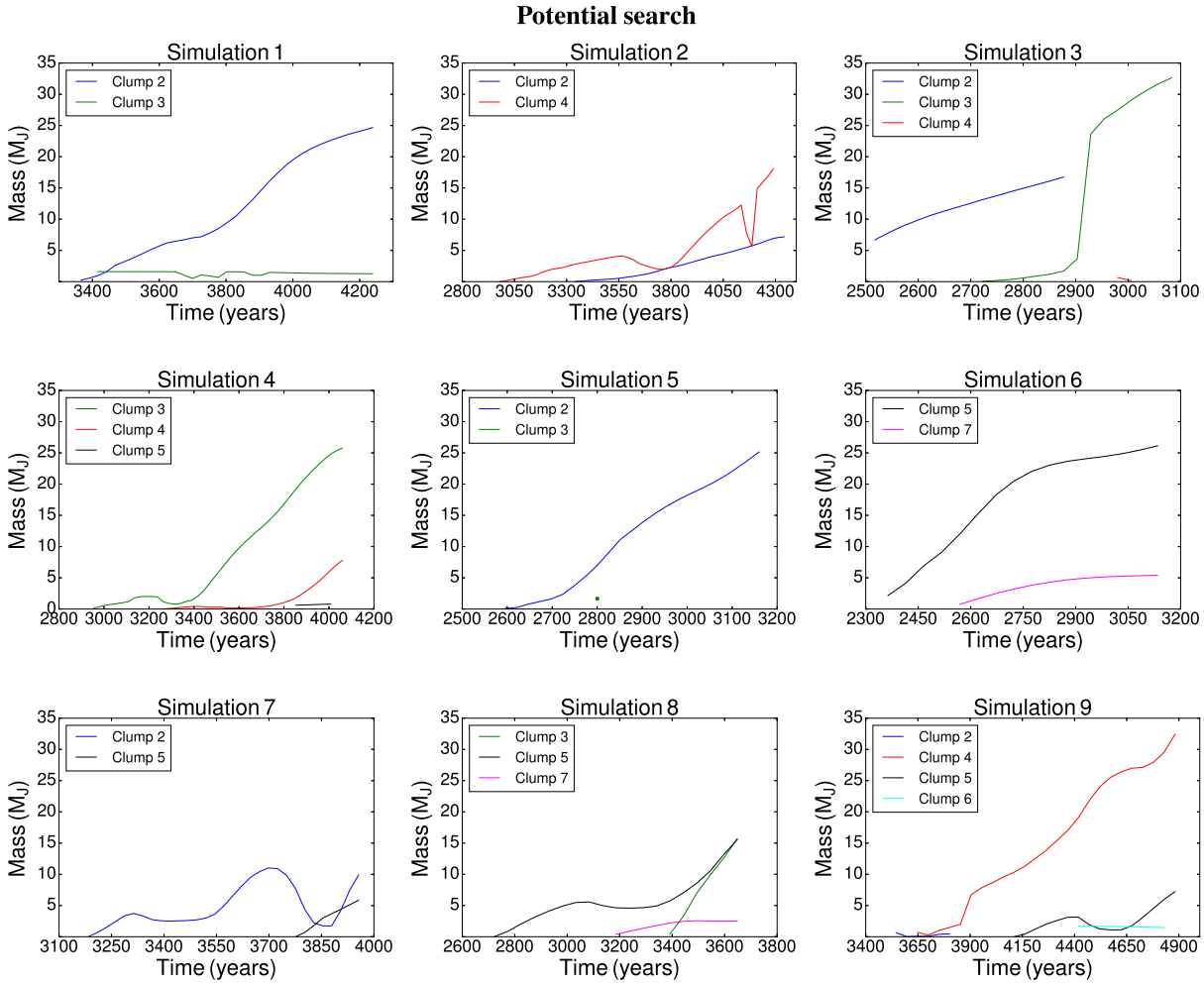

Figure 4. Mass accretion history for all clumps in all simulations, using only the ordered gravitational potential energy search. Fewer clumps are detected by this method than by using the density derivative, but those that are detected are likely to survive for a long time. Clumps are generally detected later in their evolution using this method, when their gravitational potential energy is negative enough to have neighbour particles assigned to them before they are assigned to the main body of the disc.

Additionally, our second peak is capped at $\sim$30 M_J in our simulations since this is typically when the density in a fragment becomes so high that it is computationally unfeasible to continue the simulation. With increased computation time, the mass of our largest clumps would probably increase.

Since our algorithm is quite robust at later times, detecting to within a factor of 2 the 'by-eye' clump mass in low-mass clumps (considered only in the bound region of the clump), we can see, in the final mass distribution shown in the bottom right panel of Fig. 7, that the GIPS model is significantly underestimating the fraction of planets at <5 M_J, even accounting for underestimating low-mass clumps by a factor of 2.

This can be explained by Fig. 8, which shows the mass semimajor axis distribution for the final values of the SPH clumps and the population synthesis fragments. The SPH clumps are the dark circles, and the population synthesis fragments are the light squares. As can be seen, low-mass clumps in our simulations are scattered out to large semimajor axis at these early times, and fragment–fragment interactions are likely to play an important role in the ultimate fate of a fragment. If it is scattered out to large a, it is much less likely to be tidally destroyed and far more likely to survive the duration of the simulation. This would suggest that GIPS models need to include fragment-fragment interactions in this early gas phase, since current models suggest that $\sim$40 per cent of initial fragments are tidally destroyed. If a significant fraction of these are scattered out to large radii, their survival rate could potentially be much higher.

3.3 Orbital properties

We carry out analysis of the orbital properties of our clumps only using the sample as detected by the DDS, as this method is sensitive to most clump masses and semimajor axes. The total semimajor axis evolution of all clumps is shown in the left-hand panel of Fig. 3, which we have already discussed, and refer the reader back to. Circles mark surviving clumps (including clumps that subsume another clump), squares mark destroyed clumps and triangles mark merged clumps. Larger markers correspond to more massive clumps. For destroyed clumps, we take the last measured mass. Roughly half of our most massive clumps migrate radially inwards, which is consistent with migration in locally isothermal discs, as objects exchange angular momentum with the surrounding gas and move inwards. However, about half of our most massive clumps migrate radially outwards. This is known to be possible in radiative discs (Kley & Nelson 2012), but requires either large torques or steep surface

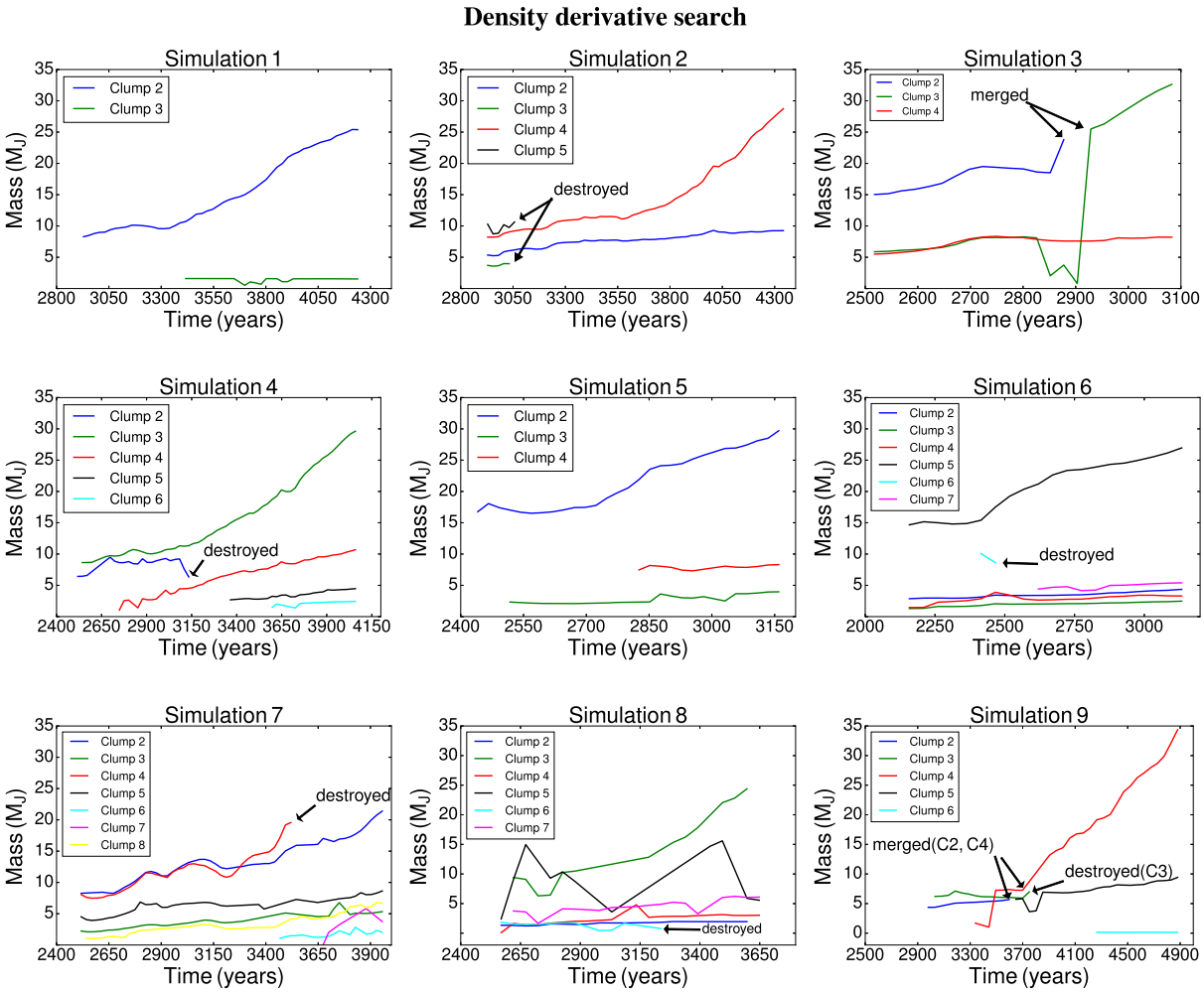

Figure 5. Mass accretion history for all clumps in all simulations, found using the density derivative search method. More clumps are detected this way than by using the ordered potential search, as clumps buried in the potential well of the disc are identified early by their density peak. As can be seen by comparison with Fig. 4, this search method is sensitive to low-mass clumps, is sensitive to all clumps earlier in their evolution, and by comparison with Fig. 3 we can see this method is also able to detect clumps which are ultimately tidally destroyed.

density gradients (D'Angelo & Lubow 2010). Large torques can have many sources, but in massive, self-gravitating discs they are likely to be in the form of global spiral arms. We carried out a Fourier analysis on the density structure of our discs, to determine the Fourier amplitude of each m mode (where m is the number of spiral arms). The amplitude, $A_{\rm m}$, of each mode, m, is calculated by

$$A_{\rm m} = \left| \sum_{i=1}^{N_{\rm region}} \frac{{\rm e}^{-im\phi_i}}{N_{\rm region}} \right|, \tag{4}$$

where $N_{\rm region}$ is the number of particles in the region we are considering (for our case, $R = 20$ to $R = 100$ au), and ϕ_i is the azimuthal angle of the ith particle. Some example amplitudes are shown in Fig. 9, which shows the first 10 Fourier components of the density structure of two discs in their initial state (i.e. when they have just begun to fragment), marked in red, and the same two discs in their final state, marked in black. The discs are from simulation 1 and simulation 5, and their final state can be seen in their column density plots, shown in Fig. 1. These discs were selected because they ran for the same length of time, and they have contrasting final m-modes states, simulation 1 ultimately peaks in the $m = 2$ mode and simulation 5 ultimately peaks in the $m = 6$ mode.

In this fashion, we determine the dominant final m mode in each disc, and plot the final semimajor axis of our clumps as a function of this m mode, in Fig. 10. We note that our decision to name a dominant mode, based on a relatively low amplitude difference, may be questioned. However, these discs are not in a quasi-steady state, having undergone fragmentation, so persistent spiral modes may be unlikely to form due to tidal disruption from these clumps. Despite the transient nature of the spiral modes, global, low m mode spiral arms can exert considerable torque, and this is clearly important for the final orbital configuration of our clumps, as shown in Fig. 10, which displays a rough empirical relationship between the maximum semimajor axis of a clump, $a_{\rm max}$, and m, such that

$$a_{\rm max} \propto \frac{1}{m}. \tag{5}$$

Of course, this relationship is preliminary, since we only consider nine discs, all of the same mass, and it has been shown that more massive discs are dominated by low m spirals (Lodato & Rice 2004, 2005). Indeed, since it has been shown that in discs without fragmentation we expect the number of spiral modes to be related to the disc-to-star mass ratio, q, such that $m \sim 1/q$ (Dong et al. 2015), to examine the full parameter space of spiral modes requires a range

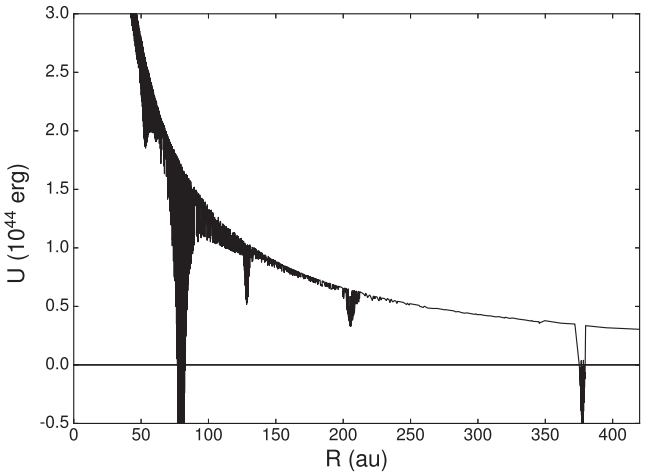

Figure 6. Radial profile of gravitational potential energy for the disc shown in Fig. 1, simulation 6. Only two clumps, at $r \sim 80$ au and $r \sim 375$ au have a sufficiently deep potential well to be identified by our ordered potential search. The other three clumps, at $r \sim 50$, $r \sim 125$ and $r \sim 210$ au are identified as belonging to the main body of the disc. Their detection in the density derivative search, but not in the ordered potential search, indicates that they would likely be tidally destroyed.

of q values. Since we consider discs with identical q values, *why* these discs have different dominant m modes is a valid question. Again, this may be explained by these discs having fragmented into bound clumps. Bound objects in a gaseous disc produce stronger, more persistent torques than spiral density fluctuations alone. If one of our clumps is scattered out of the main body of the disc, say, by interaction with another clump, it may exert a tidal torque on the material in the disc (and by Newton's third law, the material in the disc will also exert a force on the clump). Larger torques are associated with lower m modes, and if these tidal responses from the discs to the clumps is responsible for the low m-mode domination in the disc, then we expect to see steeper surface density profiles in discs with low m modes, since more mass will have been redistributed inwards as a result of this torque. This is difficult to unequivocally demonstrate in our set of simulations, since each simulation was run for a different length of time, and the amount of mass redistributed increases with time.

However, Fig. 11 shows the mass enclosed as a function of radius for the two discs plotted in Fig. 9 that ran for the same length of time. Although by no means conclusive, the slight increase in mass for a given radius between 40 and 160 au for the $m = 2$ disc in simulation 1 is consistent with tidal forces being responsible for the low m mode becoming more dominant. To properly establish the nature of the preliminary relationship detailed in equation (5) therefore requires a range of disc masses and fragmentation scenarios, and we leave this to future work. Fig. 12 shows the relationship between eccentricity, e, and semimajor axis for our SPH clumps. Larger markers indicate more massive clumps. For the most part, the more massive clumps are located on close in ($a \sim 50$ au), low eccentricity ($e \sim 0.1$) orbits, while lower mass clumps are at larger separations and with higher eccentricity. Since disc fragmentation forms objects on low eccentricity orbits ($e < 0.1$), we can see the importance of clump–clump interactions in determining the final orbital properties of a clump. Very large eccentricities ($e \sim 0.7$) at large a indicate that a clump is close to ejection, as excitations beyond unity ensure a clump is ejected from the disc. The top two panels of Fig. 13 show the initial eccentricity distribution (left) and initial inclination distribution (right) of our SPH clumps. The bottom two panels of Fig. 13 show the final eccentricity distribution (left) and final inclination distribution of the same. Inclination is calculated relative to the orbital plane of the central star, such that

$$i = \arccos\left(\frac{L_z}{|\vec{L}|}\right), \tag{6}$$

where i is the orbital inclination of the clump, $\vec{L}$ is the orbital angular momentum vector of the clump (calculated relative to the centre of mass and centre of velocity of the central star) and L_z is the z component of $\vec{L}$. Using least-squares regression, each plot has been fitted with a Gaussian of the form

$$F_p = Ae^{-\frac{1}{2}(\frac{x-\mu}{\sigma})^2} + k, \tag{7}$$

where F_p is the fraction of planets, A is the amplitude of the curve (without offset), x is either eccentricity or inclination, μ is the mean of the fitted distribution, σ is the standard deviation of the fitted distribution and k is the fitted offset constant. The fitted values are given in Table 1, and in the legend of each plot. The initial and final inclinations have been fitted with two distributions, the dotted blue line includes all points, and the solid red line does not include the most inclined point in each distribution, since there is a large gap between that point and the rest of the clumps, and a small sample size, it is unclear if this point is actually an outlier. We have provided these fits since current GIPS models do not include orbital eccentricity or inclination, and, despite our small sample size, this information may be useful in the future development of these models. Aside from a small decrease in standard deviation, there is little change between our initial and final eccentricity distribution; both peak at $e \sim 0.1$ and share an offset constant of $k = 0.006$. However, the orbital inclination of our clumps is reduced by a factor of ∼100 between the initial and final states, showing that clump orbital inclination, in our SPH simulations, is rapidly reduced after formation. Considering that many of our clumps undergo dynamical interactions that cause scattering and eccentricity pumping on short time-scales, this high degree of coplanarity may be surprising, especially when considering that most exoplanets have mutual inclinations of a few degrees (Figueira et al. 2012; Fang & Margot 2013). However, it is consistent with our current understanding of highly inclined planet orbits relying on dynamical perturbations such as the Lidov–Kozai mechanism (Naoz et al. 2013). Our results may indicate that developing inclined orbits is difficult while a gas disc is present, even if substantial dynamical interactions between clumps take place in this time.

3.4 Spin properties

We analysed all of the fragments in our simulations, and found that several of them survive to the end of the simulation whilst undergoing retrograde rotation. This is shown in Fig. 14, which shows the relative alignments between the orbital angular momentum vector and the rotational angular momentum vector of the clumps. Both the top and bottom panel is split into two parts, showing significant disalignment at the top, marked in red crosses, and good alignment at the bottom. The top panel shows the alignment as a function of mass, and the bottom panel shows the alignment as a function of semimajor axis.

This prompts the question – how did they get to be retro-rotating? Did they form like this, or were they perturbed in some way? Having checked all of the clumps with significant disalignment, we can see that all of them were perturbed by a close encounter with another

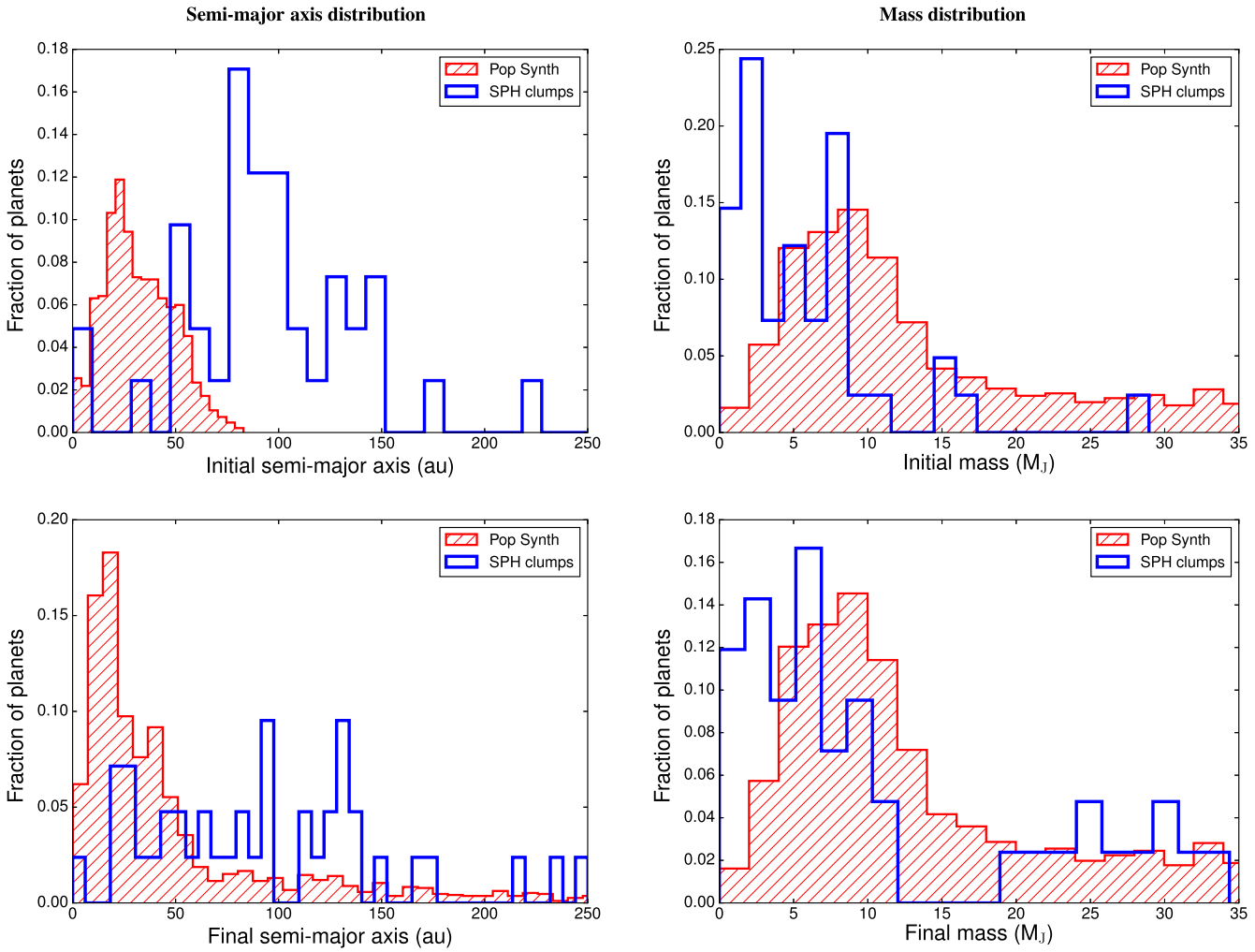

Figure 7. Left column shows initial (top) and final (bottom) semimajor axis distribution for our SPH clumps and the population synthesis model of Forgan & Rice (2013). Right column shows the initial (top) and final (bottom) mass distribution for the same. Population synthesis data are shown in hatched red, while blue outline shows SPH clumps. Our initial mass and semimajor axis distributions are not strictly accurate, due to limitations of the algorithm requiring a threshold to be met before identification. However, our algorithm is quite robust at later times, and our final semimajor axis distribution shows the importance of clump–clump interactions in the final configuration of a system, with many clumps at large separations due to interactions with each other. Our final masses below 5 M_J are typically underestimated by a factor of 2 what would be identified as mass belonging to the clump 'by-eye', and accounting for this shows a final mass distribution not unreasonably dissimilar to what we should expect from GI population synthesis models, given the small N statistics we are considering.

fragment, which typically flung them rapidly further out into the disc. We give the most extreme example in Fig. 15, which shows the retro-rotating clump 4 in simulation 4. In the leftmost panel, we see in the bottom left corner two clumps undergoing a close encounter. One of them then decreases its semimajor axis, whilst the other one is flung further out into the disc, to become retro-rotating. Fig. 16 shows the specific angular momentum profiles of a retro-rotating clump (top) and a prograde-rotating clump (bottom). The blue line, at $T = 2788$ yr, is as soon is the clump is detected by our algorithm. We can see that the majority of the clump is in prograde rotation, with only the outer $\sim$1 au in retrograde rotation. However, as time progresses and the clump continues to accrete material that is retro-rotating due to the encounter, this ultimately changes the rotation of the whole clump. For comparison, the bottom panel contains a prograde rotator of similar mass from simulation 5.

Fig. 17 shows the rotation velocity profiles of two clumps. Top shows the ultimately retro-rotating clump 4 in simulation 4, and the bottom, for comparison, is a clump of comparable mass that is always undergoing prograde rotation. Negative velocity is determined by the orbital angular momentum vector of the whole clump and the rotational angular momentum vector of the material being anti-aligned. Both panels show the clumps at four different times, and the dashed lines indicate the breakup velocity profile of each clump. Both clumps are rotating under their breakup velocity for radii below 1 au, and their velocity profiles are consistent with solid body rotation (i.e. $v \propto R$) at these radii. Much further out, the clumps become nebulous, but we have included information out as far as possible to show the interesting angular momentum exchange between material at $T = 2788$ and $T = 3377$ yr for the retro-rotator. For the prograde rotator, the ultimate configuration is a good approximation to a solid body rotation curve out to extended radii ($\sim$3 au). Interestingly, for the retro-rotator, the velocity profile at the outer part of the fragment ($\sim$2.2 to $\sim$4 au) is consistent with Keplerian rotation (i.e. $v \propto 1/\sqrt{R}$). This suggests the presence of a disc, or a disc-like structure, around the clump. Unfortunately, it is not (at the time of writing) currently possible to self-consistently re-resolve such regions in SPH simulations, so we are unable to investigate this further.

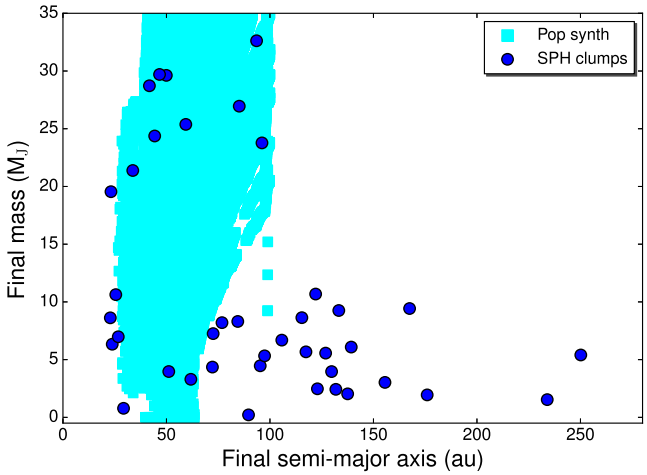

Figure 8. Final mass semimajor axis relation for our SPH clumps (dark blue circles) and Forgan & Rice (2013) fragments (light blue squares). We can see a dearth of intermediate mass SPH clumps at 15–25 M_J. However, since we are dealing with a small sample size we cannot say for sure if this is statistically significant. Despite the small sample size, we can see that large separations for low-mass objects are much more common than suggested by population synthesis models.

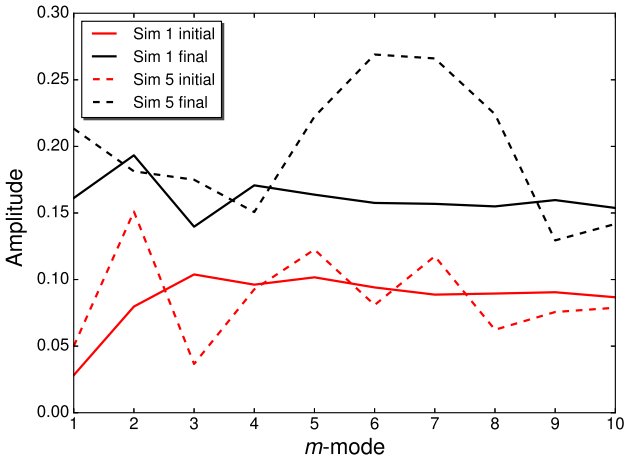

Figure 9. Amplitude of the first 10 Fourier components of the density structure of the discs in simulation 1 and simulation 5, calculated between $R = 20$ and $R = 100$ au, at their initial state (when they have begun to fragment), marked in solid lines, and their final state, marked in dashed lines, at the last time-step.

3.5 Density and temperature properties

Maximum density and temperature for all clumps in our simulation is shown in Fig. 18, open circles show prograde-rotating clumps and dark triangles show retrograde-rotating clumps. The maximum temperature we identify in a clump is 2081 K, which implies that none of our fragments have started to dissociate molecular hydrogen and can therefore be considered as the first hydrostatic cores. Additionally, a further nine clumps have internal maximum temperatures above ∼1000 K, which means they would begin to evaporate dust. Both of these results are in good agreement with previous studies of fragments, such as Vorobyov et al. (2013), who found similar results. Our measurements of clump maximum temperature are limited by our resolution, since running simulations at higher resolution would allow higher densities to be reached before becoming computationally infeasible to continue.

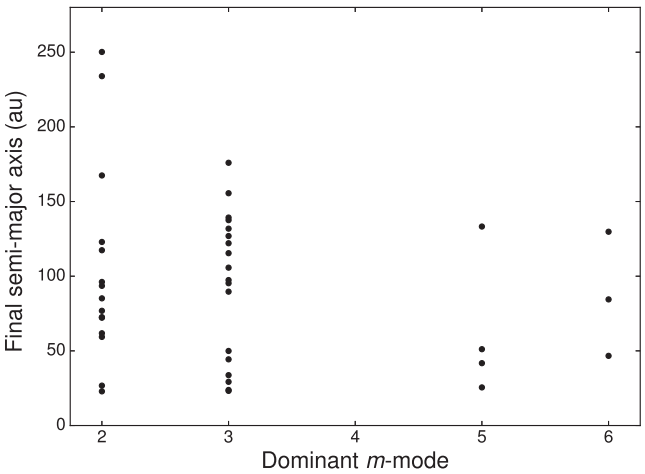

Figure 10. Final semimajor axis of all clumps in all simulations as detected by the density derivative search, as a function of the dominant m mode in the disc. The largest semimajor axis requires a 2 armed spiral, which is capable of exerting global torques. There appears to be a rough empirical relationship such that the maximum semimajor axis $a_{max} \propto 1/m$, although this result is preliminary due to a small number of data points.

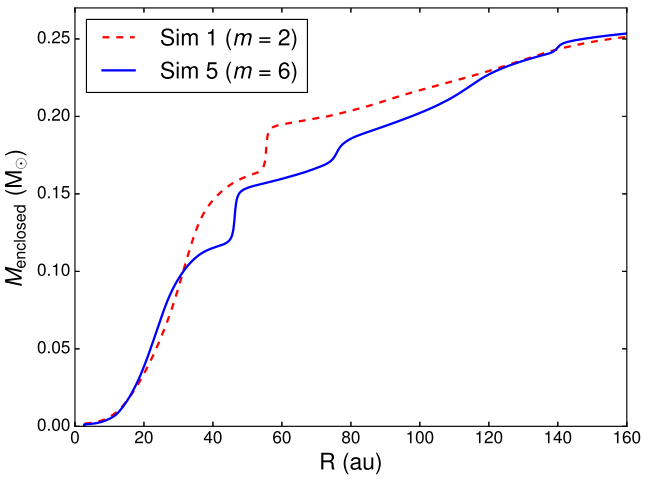

Figure 11. Disc mass enclosed as a function of radius for the final time-steps of simulation 1 (red dashed line) and simulation 5 (blue solid line). Since more mass is enclosed at shorter radii for simulation 1, more mass has been transported inwards in the disc, giving it a slightly steeper density profile.

As discussed in our introduction, the advantage of using a purely hydrodynamical simulation with no sink particles is that we can examine fragment internal structure during the simulation. With this in mind, we show the radial temperature and density profiles of seven fragments, one of which ultimately becomes the hottest fragment in our simulations, shown in Fig. 19, and the remaining six are three retro-rotators and three prograde rotators, of comparable mass and with similar simulation histories, shown in Fig. 20. In both figures, each image is split into two panels, radial temperature profile on the top and radial density profile on the bottom. The initial clump profile is shown in solid red, and the final clump profile is shown in solid blue. For comparison, a polytrope is also plotted in each panel.

Fig. 19 shows the radial density and temperature profile of the hottest clump identified out of our nine simulations. We can see that although the radial temperature profile is well described by a

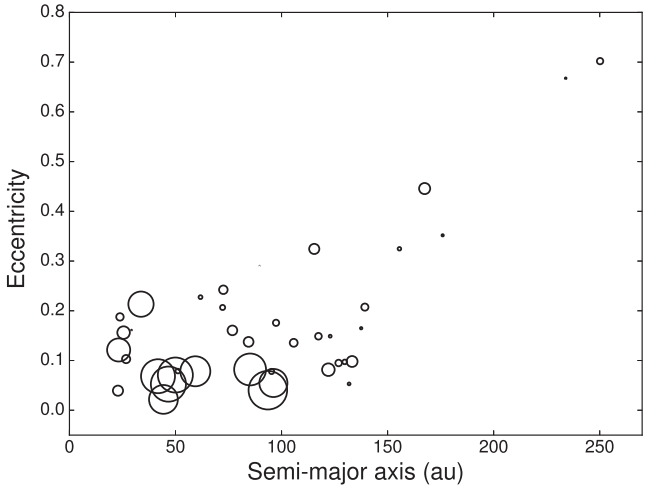

Figure 12. Final semimajor axis and eccentricity relation for our SPH clumps. Larger markers represent more massive clumps. The population synthesis model does not contain eccentricity data. We can see, for the most part, our clumps have a roughly linear relationship between eccentricity and semimajor axis, although there is a large amount of scatter.

polytrope of index $n = 1.6$, for the initial state, and $n = 1.8$ for the final state, in both cases the actual density deviates from the polytropic density significantly. This is also true for the rest of the clumps, shown in Fig. 20, where the left-hand column shows prograde rotators, and the right-hand column shows retrograde rotators. In all cases in Fig. 20, we have plotted a polytrope of index $n = 1.5$, which is appropriate for a fully convective star such as a brown dwarf. Since in a polytrope, pressure P and density ρ are related by

$$P = K\rho^{\frac{n+1}{n}}, \tag{8}$$

where K is a constant and n is the polytropic index, it implicitly assumes that pressure is a power-law function of density which is constant throughout the star. For our clumps, it appears to be the case that a polytropic approximation may be too simplistic when estimating the internal structure of the clump. This may have some implications again for current GIPS models, since orbital parameters are sensitive to the radial distribution of mass in the forming fragments. It is probably best to exercise caution when constructing clumps in GIPS models, and it may be the case that a 'follow the adiabats' approach, as used in Nayakshin & Fletcher (2015), is more appropriate.

When we compare the final states of the retro-rotating clumps with their prograde-rotating counterparts, there is not much that would mark them as retro-rotating, final density and final temperature profiles for both directions of rotation are similar, and are consistent with other simulations of fragmenting protostellar discs (see e.g. Vorobyov et al. 2013). There is one clump that is an exception when compared to the rest of the clumps, and is shown in the top right-hand panel of Fig. 20. This is S4C4. In its final state, the surface temperature of the clump is a factor of ∼3 higher than we see in the rest of the clumps, and its central temperature is ∼425 K, a factor of ∼2 larger when compared to the rest of the clumps in Fig. 20. This high temperature could possibly be explained by an encounter with another clump. Fig. 15 shows this interaction, (clump 4 is marked by a green square). It is scattered by the more massive clump into the outer part of the disc, becoming shocked as it passes through a spiral arm. The encounter with the other clump causes the direction of rotation of clump 4 to change, but the large increase in temperature could be due to this motion through a region of increased density, entering perpendicular to the spiral arm where the density gradient is at its largest.

We suggest therefore that clump-clump interactions may provide a mechanism for dramatic increase in temperature of forming clumps, either directly through the interaction, or their subsequent scattering through dense regions in the disc. This mechanism could present a problem for terrestrial planet formation through tidal downsizing. For a terrestrial planet to form in the tidal downsizing scenario, a clump must not accrete too much mass, and then become tidally disrupted after migrating too close to the host star (Nayakshin 2010; Boley et al. 2010). It then leaves behind a solid core, *if* dust grain sedimentation was sufficiently rapid to form a core. Since we have tentatively shown that clump–clump interactions are common (given our small sample size), then it may be possible that clump temperatures are frequently too high, at too young an age, for dust sedimentation to have taken place inside clumps. For a solid core to form, clumps need to exist at a temperature below the dust sublimation temperature (∼1200 K) for the duration of the sedimentation process.

3.6 Tidal disruption and mergers

Of the 41 clumps detected by the DDS method in our simulations, seven were tidally destroyed by the central star, and four clumps underwent mergers. Despite our small sample size, these results suggest that both tidal destruction and mergers are common amongst protostellar disc fragments. An example merger is shown in Fig. 21, which shows simulation 3, clumps 2 and 4, merging together. An example tidal disruption is shown in Fig. 22, which shows simulation 7, clump 4 undergoing tidal disruption. Such tidal disruptions could potentially be an explanation for outburst type behaviour in young protostars, due to the rapid increase in accretion rate on to the central star (see e.g.Vorobyov & Basu 2005; Boley et al. 2010; Nayakshin & Lodato 2012). We leave observational signatures of our tidal disruptions to future work.

4 DISCUSSION AND CONCLUSION

In this paper, we have presented one original method for identifying fragments in a simulation, the DDS, and one method adapted from the `CLUMPFIND` (Williams et al. 1994; Smith et al. 2008; Forgan et al. 2016) algorithm. We ran nine SPH simulations of a 0.25 $M_\odot$ disc around a 1 $M_\odot$ star, each with a surface density profile of $\Sigma \propto r^{-1}$, an inner radius of 10 au and an outer radius of 100 au. Each simulation was run for as long as computationally feasible without converting dense regions to sink particles, since we wished to calculate orbital properties for our fragments, which are sensitive to their radial mass distribution.

Each disc fragmented to form at least two bound objects, and we analysed the fragments (which we call clumps, once they have been detected) using the DDS and the adapted `CLUMPFIND` method. We have shown that these two methods are complementary, as the DDS is able to detect low-mass clumps, and clumps that are ultimately tidally destroyed, while the search using the adapted `CLUMPFIND` method filters out clumps which are unlikely to survive the simulation, but also has a relative insensitivity to low-mass clumps.

We compare our sample of fragments to the population synthesis model of Forgan & Rice (2013), and find that our algorithm has some limitations at early times (i.e. during the initial period of fragment formation), which means that some radial migration has

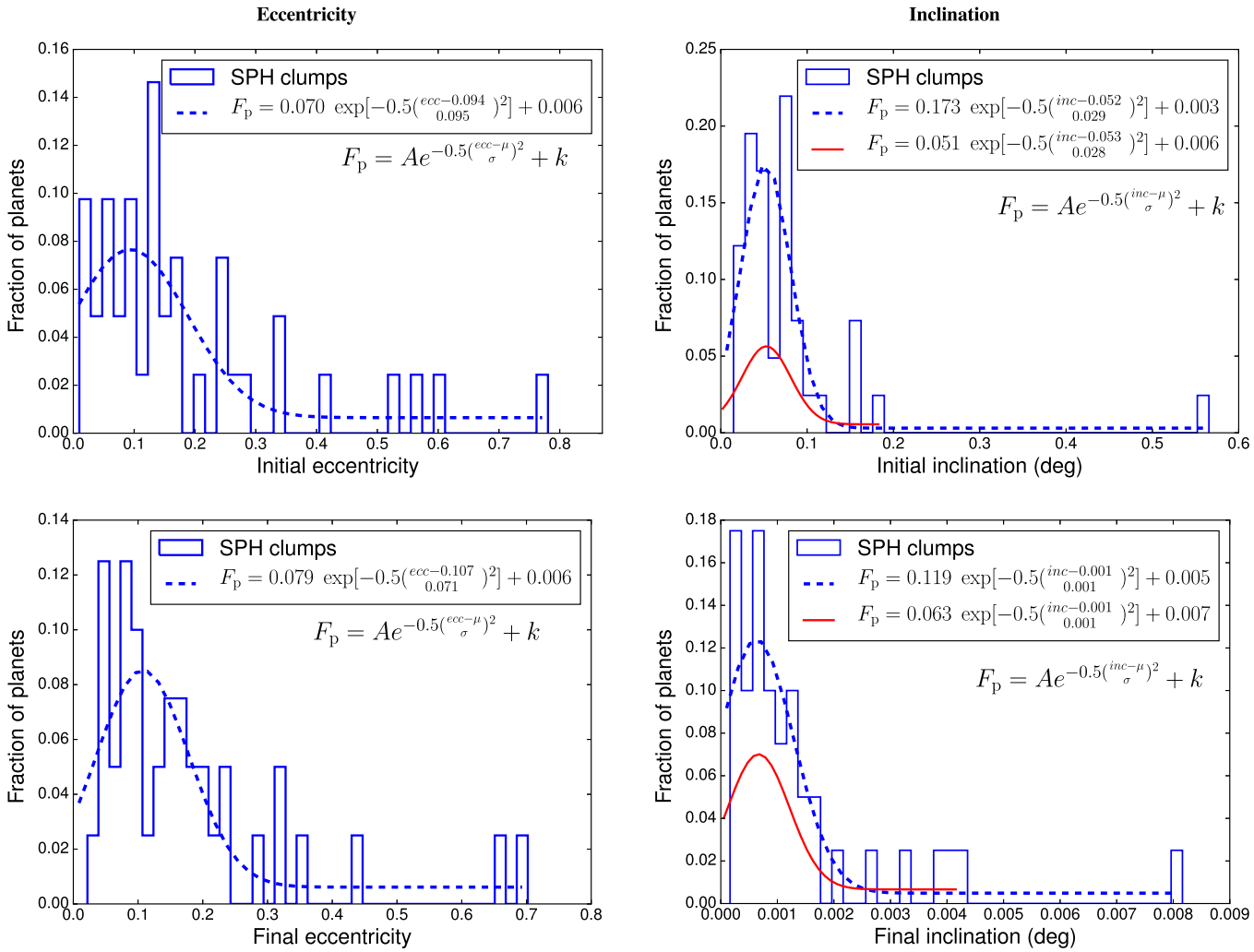

Figure 13. Left column shows initial (top) and final (bottom) eccentricity distribution for our SPH clumps. Right column shows the initial (top) and final (bottom) inclination distribution for the same. Inclination is calculated relative to the orbital plane of the central star. Since the population synthesis models of Forgan & Rice (2013) do not contain eccentricity or inclination information, we do not plot them here. Using least-squares regression, we have fitted our distributions with a Gaussian of the form $F_p = A\exp[-0.5(\frac{x-\mu}{\sigma})^2] + k$, where F_p is the fraction of planets, A is the amplitude of the curve (without offset), x is eccentricity or inclination, μ is the mean of the distribution, σ is the standard deviation and k is the offset constant. The fitted values are given in Table 1 and in each plot legend. We have included these fits since we consider they may be useful in developing future GI population synthesis models, but caution that our sample size is small. Our inclination histograms have been fitted with two distributions. The dotted blue line includes all data points, and the solid red line does not include the most inclined point in each distribution, since with a small sample size, and an apparent gap between the rest of the clumps, it is unclear whether or not this is an outlier. There is little change between our initial and final eccentricity distribution, both peaking at $e \sim 0.1$, and a slightly smaller standard deviation for the final configuration. The inclinations of our clumps are decreased by a factor of ~ 100 between their initial and final states, showing that clump orbital inclination is rapidly adjusted after formation, until it orbits almost entirely in the plane of motion of the central star.

Table 1. Parameter values of the Gaussian fits applied to the histograms in Fig. 13. From left to right, the columns are plot, mean, standard deviation, amplitude (without offset) and offset constant.

Plot	μ	σ	A	k
Initial ecc.	0.094	0.095	0.070	0.006
Final ecc.	0.107	0.071	0.079	0.006
Initial inc. (no outlier)	0.052	0.029	0.173	0.003
Initial inc. (with outlier)	0.053	0.028	0.051	0.006
Final inc. (no outlier)	0.001	0.001	0.119	0.005
Final inc. (with outlier)	0.001	0.001	0.063	0.007

already happened before the algorithm detects the fragment. Despite this, it is fairly robust at late times (i.e. a few orbital periods after formation), and so our final mass and final semimajor axis functions, and the mass semimajor axis relationship, are representative of the final configurations (i.e. at $T \sim 4000$ yr) of our systems. Of course, the final mass and final semimajor axis distributions that we present here will differ from the *ultimate* distributions of the systems. These will only be determined some $\sim 10^6$ yr after formation, long after the disc has dispersed. What happens after disc dispersal is not considered in this work, but we refer the interested reader to Forgan, Parker & Rice (2015) and Li et al. (2016).

We examine the internal temperature and density structure of our fragments, and compare them with appropriately indexed polytropes. We find that the central density of our fragments are typically

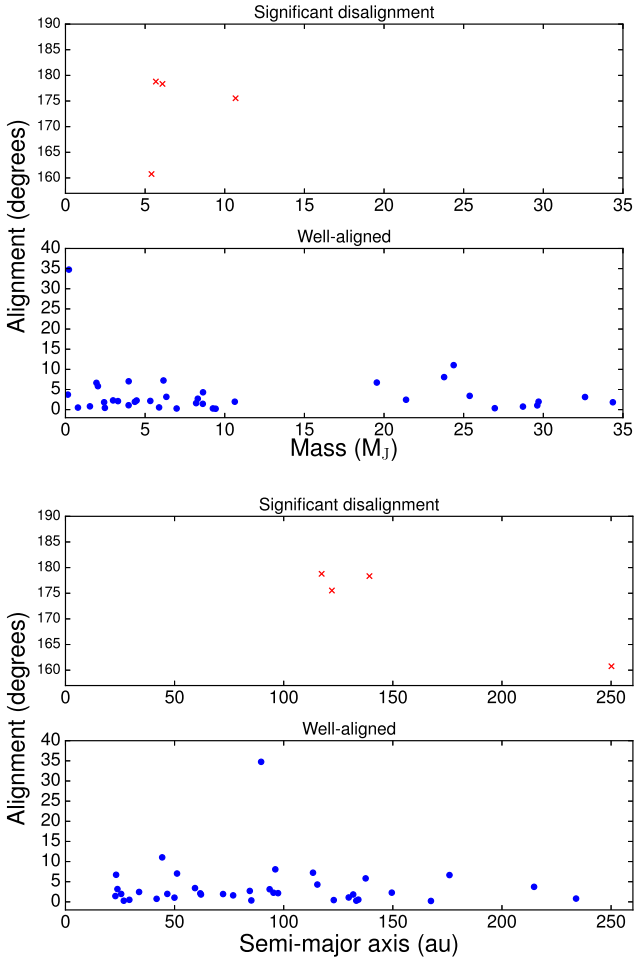

Figure 14. All plots show alignment, on the *y*-axis, defined as the angle between the orbital angular momentum vector and the rotational angular momentum vector. Top two panels show alignment as a function of mass, bottom two panels show alignment as a function of semimajor axis. The plots are split, for clarity, into two different regions, between 0° and 40° and between 155° and 190°. Well aligned clumps are marked by blue circles, clumps with a significant degree of disalignment are marked with red crosses. Both plots show that four low-mass, high-separation clumps are retro-rotators, given that all of them or orbiting in prograde motion.

an order of magnitude denser than their polytropic equivalent, and since orbital parameters of a body are sensitive to its internal mass distribution, we recommend caution when using polytropes in GIPS models to calculate orbital parameters.

Furthermore, that the interiors of the clumps may not be well described by polytropes may raise concerns about the validity of the Forgan et al. (2009) hybrid radiative transfer method, which uses the polytropic cooling formalism of Stamatellos et al. (2007) to approximate radiative cooling. Essentially, the assumption is that each SPH particle is embedded in its own polytropic pseudo-cloud, of polytropic index n. Therefore, the cooling of any morphology that is not a polytrope of index n may not be exactly described by the polytropic cooling formalism. However, so long as the geometry is *approximately* spherical, which gravitationally bound clumps tend to be, then the polytropic cooling approximation is valid to within an order of unity for a variety of opacity laws (Wilkins & Clarke 2012).

More generally, the polytropic cooling method of Stamatellos et al. (2007) has been criticized when employed in planar geometry, such as in self-gravitating protostellar discs. The most alarming of these is the systematic underestimation of cooling rates by a factor of ∼100 (Wilkins & Clarke 2012), due to the use of local variables only in optical depth determination. This ignores the decreasing column density normal to the mid-plane of the disc, which may offer an easier escape path for photons.

However, this criticism is specific to the polytropic cooling method of Stamatellos et al. (2007), rather than the hybrid method of Forgan et al. (2009). By including flux limited diffusion, the problems outlined in Wilkins & Clarke (2012) are addressed.

More recently, the polytropic cooling approximation of Stamatellos et al. (2007) has been updated to include radiative feedback from sink particles (Stamatellos 2015), which is not captured by the Forgan et al. (2009) hybrid scheme. However, we do not use sink particles in this work, since we aim to characterize the radial properties of our fragments. By using only SPH particles, the flux limited diffuser in the Forgan et al. (2009) algorithm naturally provides radiative feedback from the fragments, as heat is diffused from hotter to cooler regions.

Ultimately, the hybrid method of Forgan et al. (2009) is an approximation to a computationally much more expensive task, a full radiation hydrodynamical treatment of disc evolution. Therefore, results obtained using this approximation should be adopted with knowledge of its limitations in mind.

The radiative cooling of real protoplanetary discs depends strongly on opacity, which is not examined in this work. Dust opacities have a large degree of uncertainty; for temperatures below ∼1000 K, dust grains dominate absorption, so this uncertainty is likely to matter in the region of parameter space considered in this work. For example, Semenov et al. (2003) have shown that for temperatures 100 K $< T <$ 1000 K, opacity may differ by a factor of ∼10. Since it is known that initial fragment mass depends on opacity

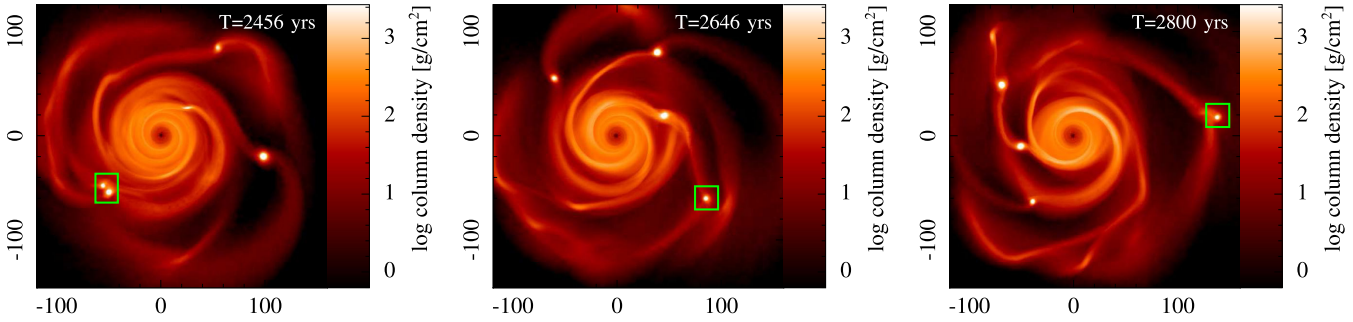

Figure 15. Column density plots of simulation 4, increasing in time from left to right, showing clump 4 (marked by green square), an initially prograde-rotating clump, undergoing an encounter with another clump to become a retro-rotating clump.

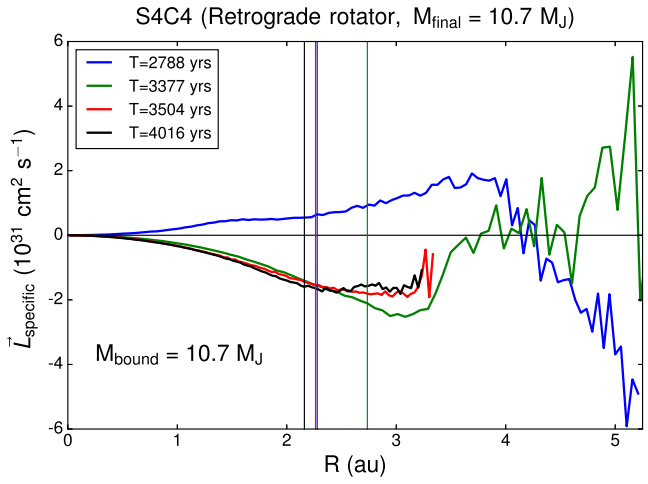

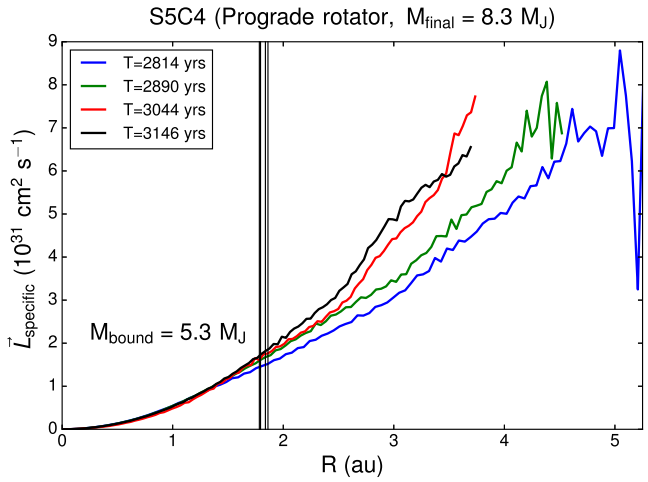

Figure 16. Top: radial profile of specific angular momentum for an example retro-rotating clump (clump 4, simulation 4), at four different times. Horizontal lines indicate the last bound point of the clump at times indicate in the legend. The final bound mass is marked on the plot, and in this case, all of the mass that is identified as belonging to the clump is ultimately bound to the clump. Positive values for $\boldsymbol{L}_{\rm specific}$ indicate that the rotational angular momentum vector of the material and the orbital angular momentum vector of the whole clump are aligned (or at least inclined at less than 90°), and negative values indicate that the two vectors are anti-aligned. The blue line is when the clump is first detected, and we can see that the majority of the clump is in prograde rotation, and the outer $\sim$ 1 au is in retrograde rotation. The material came to be retro-rotating due to a close encounter with another clump, which is shown in Fig. 15. As the clump continues to accrete material, we can see that angular momentum is exchanged between the inner material and the outer material (green line, $T = 3377$ yr). As the clump contracts, this positive angular momentum material is no longer considered part of the clump. Bottom: for comparison, the specific angular momentum profile of a clump of comparable mass undergoing prograde rotation (clump 4, simulation 5). The horizontal line indicates the last bound radius in the clump for the four clumps, only one line is plotted here as the four are so close together. The final bound mass of the clump is stated on the plot.

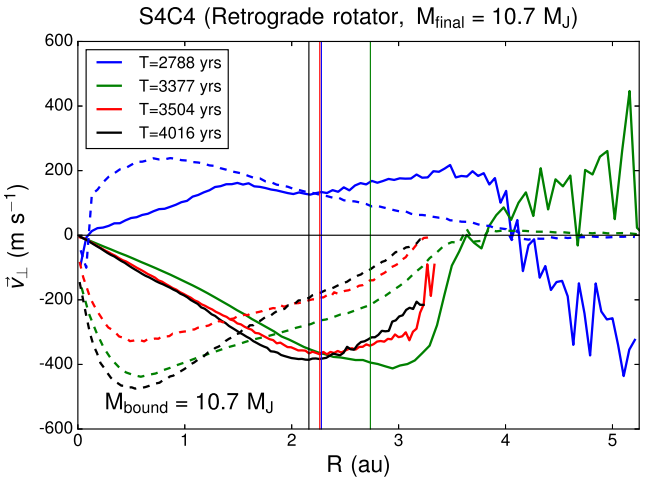

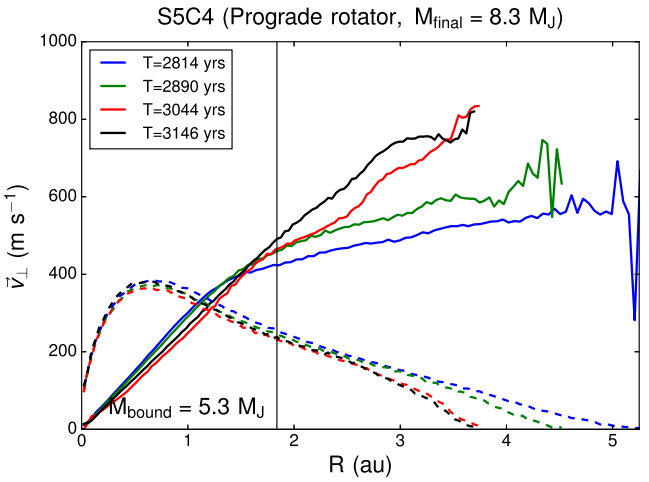

Figure 17. Top: rotation velocity curve for an example retro-rotating clump (clump 4, simulation 4), at four different times. Horizontal lines mark the last bound radius in the clump at times given in the legend. In this case, the total bound final mass is equal to the total mass ultimately identified for the clump. Dashed lines correspond to breakup velocities at these times. Negative velocities indicate that the rotational angular momentum vector of the material and the orbital angular momentum vector of the whole clump are anti-aligned (or at least inclined at more than 90°) relative to each other. We can see that beyond $\sim$1.5 au, the material is rotating at faster than its breakup velocity, which would perhaps suggest that material is spreading outwards from the clump, in a disc-like, or toroidal, manner. Bottom: for comparison, a clump of comparable mass undergoing prograde rotation (clump 4, simulation 5). Again, beyond $\sim$1 au, rotation velocity exceeds breakup velocity, and so we may expect to see a considerable spread of material around such an object, morphologically similar to a toroid.

(Masunaga & Inutsuka 1999), our initial fragment mass distribution may differ from what we state here.

However, it is widely accepted that dust opacity is proportional to metallicity, and it has been shown that while low-metallicity fragments may be a factor of $\sim$3 more massive than solar metallicity fragments, the initial mass distribution of the fragments is, apart from the shift at low mass, very similar between the two metallicities (Bate 2005). We conclude, in light of this, that our fragment mass distributions are probably reasonable, but caution that the lower mass fragments may be larger if opacity is decreased. It is possible to estimate the mass dependence on opacity by appealing to the opacity limit for fragmentation, as follows.

Usual derivations of the opacity limit for fragmentation include an *efficiency factor*, e, which subsumes, amongst other unknowns, the opacity of the gas. Adjusting this efficiency factor allows us to

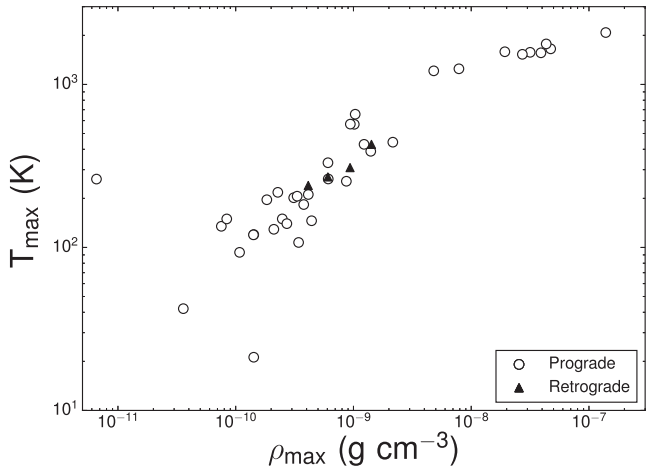

Figure 18. Final maximum temperature and density of clumps in all simulations. Open circles are prograde-rotating clumps, closed triangles are retrograde-rotating clumps.

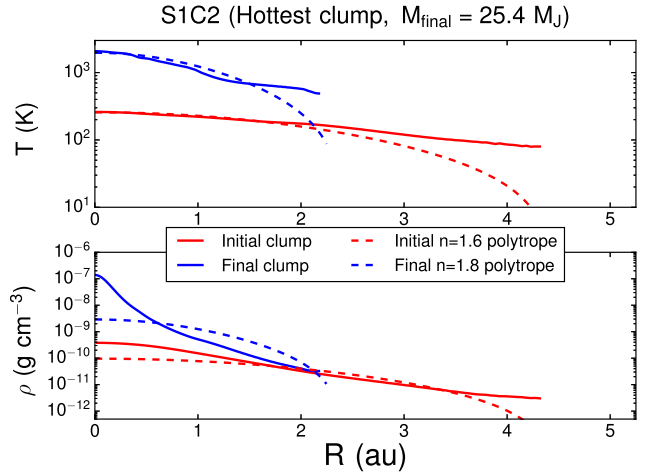

Figure 19. Radial temperature and density profile of the hottest clump we identified in our simulations, clump 2 in simulation 1. Red solid lines show initial temperature and density, blue solid lines show final temperature and density. For comparison, an $n = 1.6$ polytrope is plotted for the initial clump, and an $n = 1.8$ polytrope is plotted for the final clump. In both cases, the polytrope is a good fit to the temperature profile of the clump, however it is a poor fit to the density, particularly in the final state, where it underestimates central density by almost two orders of magnitude.

examine a range of potential fragment masses. We begin with an expression for the power of a ball of gas collapsing in free-fall:

$$\frac{|B|}{t_{\rm ff}} = \left(\frac{3}{5\pi}\frac{\mathrm{G}^3M^5}{R^5}\right)^{\frac{1}{2}}, \tag{9}$$

where B is the gravitational binding energy of the gas, given by

$$B = -\frac{3}{5}\frac{\mathrm{G}M^2}{R}, \tag{10}$$

and $t_{\rm ff}$ is the free-fall time of the gas, given by

$$t_{\rm ff} = \sqrt{\frac{3\pi}{32\mathrm{G}\rho}}. \tag{11}$$

For the collapse to continue isothermally, then

$$\frac{|B|}{t_{\rm ff}} \lesssim L, \tag{12}$$

where L is the luminosity describing the radiation of the ball of gas, as a blackbody, given by

$$L = e4\pi R^2\sigma T^4, \tag{13}$$

where T is temperature, σ is the Stefan–Boltzmann constant and e is the *efficiency factor* of the radiation. Substituting our expression for power, $|B|/t_{\rm ff}$, and luminosity, L into equation (12), we can rearrange equation (12) to arrive at an expression for the *critical mass*:

$$M_{\rm crit} = \left(\frac{400}{9}\frac{e^2\pi^4\sigma^4T^8R^9}{\mathrm{G}}\right)^{\frac{1}{5}} \tag{14}$$

above which the collapse proceeds adiabatically. However, this mass must be above the local *Jeans mass*, $\mathrm{M_{Jeans}}$, for the collapse to continue, so we now have a condition

$$\mathrm{M_{Jeans}} \lesssim M \lesssim M_{\rm crit}, \tag{15}$$

which must be satisfied. If $\mathrm{M_{Jeans}}$ and $M_{\rm crit}$ are equal, we then arrive at the *opacity limit for fragmentation*, which describes the minimum mass of a fragment that may form. Inserting constants, we now have an expression for the minimum fragment mass,

$$M_{\rm frag} \approx 6\frac{T^{\frac{1}{4}}}{e^{\frac{1}{2}}}\,\mathrm{M_J}. \tag{16}$$

From this, we can see that for a fixed temperature, minimum fragment mass increases with a decrease in efficiency. If the efficiency of the radiation is 100 per cent, i.e. the gas has a sufficiently low opacity such that it is effectively completely optically thin to escaping radiation, then for a temperature of $T \sim 10$ K a fragment mass of $\sim$10 $\mathrm{M_J}$ is expected. For an efficiency of 20 per cent, then this rises to $\sim$23 $\mathrm{M_J}$. Clearly, how strongly this efficiency depends on opacity will determine the relationship of proportionality, however, it is clear that opacity plays an important, if not dominant, role in determining initial fragment mass. In addition to determining initial fragment mass, the opacity will also play an important role in determining the final fragment mass through accretion rate on to the fragments, since the thermodynamics of the gas inside the Hill sphere of the fragment depends on this opacity (Stamatellos 2015).

We find that fragment–fragment interactions play a substantial role in the ultimate fate of our systems. Low-mass fragments can be scattered out to large radii (and therefore remain low mass, since there is less material to accrete), and are therefore unlikely to be tidally destroyed by the central star. Since current GIPS models suggest that $\sim$40 per cent of initial fragments are ultimately tidally destroyed (Forgan & Rice 2013), if a significant number of these fragments are actually scattered out to large separations by interactions with other fragments, this figure could potentially be much lower. We therefore recommend that fragment–fragment interactions in the gas phase of the disc be included in any new GIPS models.

During their lifetime, we find that our fragments may be shocked as they pass through spiral arms, rapidly increasing the internal energy of the fragment. This could have implications for terrestrial planet formation through the tidal downsizing hypothesis, since solid core formation requires rapid dust sedimentation. If the interior of these fragments are hot enough to sublimate dust at very early stages in their lifetime, it may not be possible for them to form solid

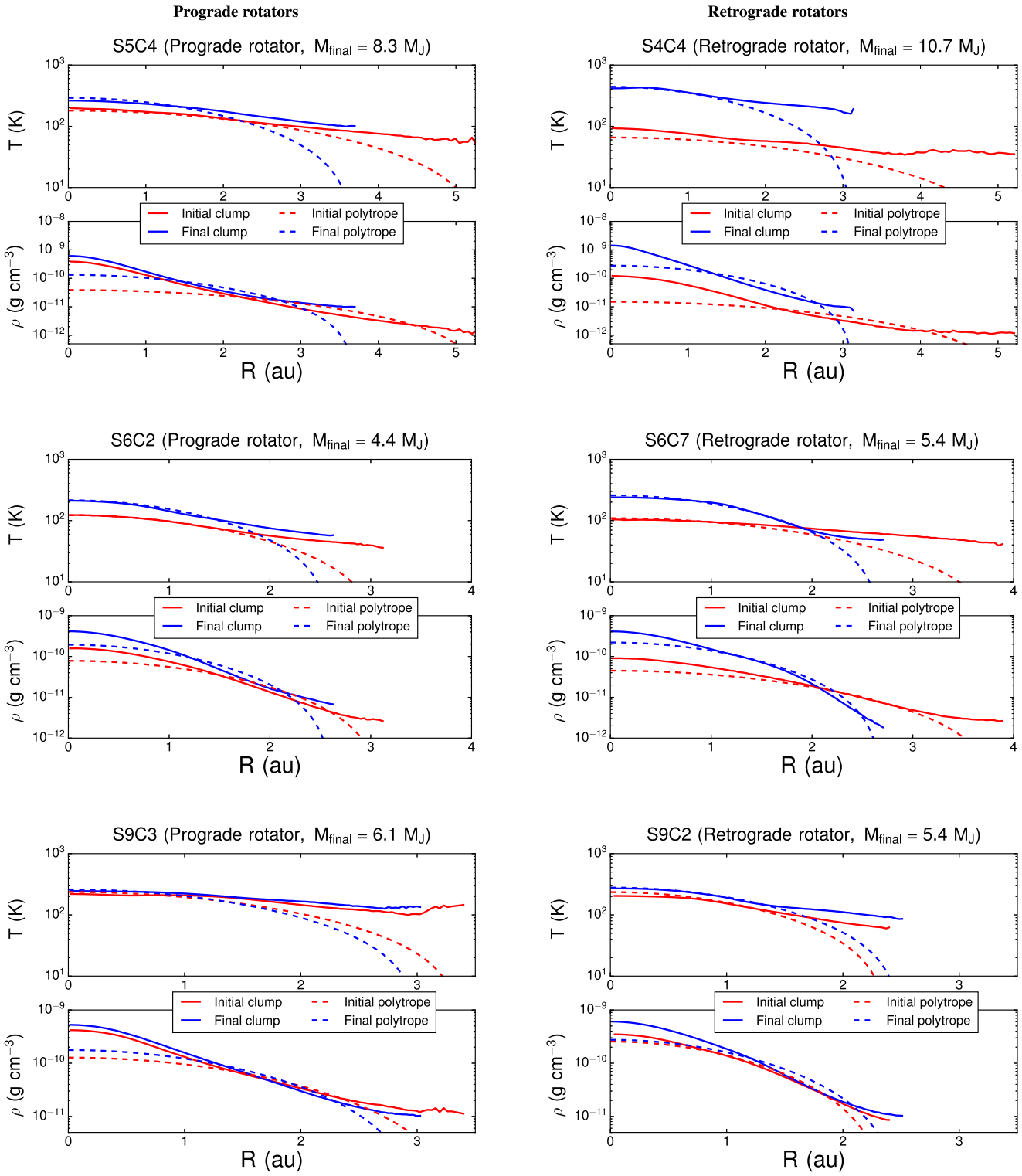

Figure 20. Radial density and temperature profiles for the initial and final state of six clumps. Red solid lines show initial clump profile, blue solid lines show final clump profile. For comparison, all clumps have initial and final $n = 1.5$ polytropic profiles plotted in initial and final states. The left column contains three clumps undergoing prograde rotation, and the right column shows three clumps undergoing retrograde rotation. In each row, the clumps are of comparable mass, and are intended to be compared, although bearing in mind that the clumps have had different evolutionary histories and their final masses are not identical. For most of the clumps, there is not much in their profiles that would mark them as a retro-rotating clump. The final inner and surface temperatures are similar, as is the shape of the density profile. Clump 4 in simulation 4 (top right panel) is somewhat the exception, with a large increase in both final inner density, inner temperature and surface temperature. Given the violent encounter it endured early in its history (shown in Fig. 15), this may be unsurprising, but it is interesting to note that high surface temperatures may indicate a violent encounter in the past. In all cases, a polytrope of index $n = 1.5$ is a reasonable fit to the temperature profile, but consistently underestimates the inner density by around an order of magnitude.

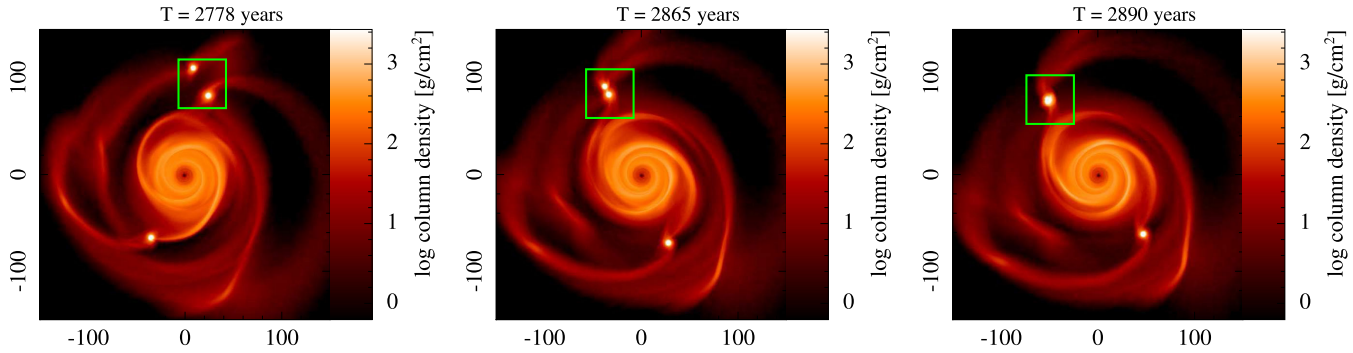

Figure 21. Column density plots of simulation 3, where clumps 2 and 4 (highlighted in green) undergo a merger.

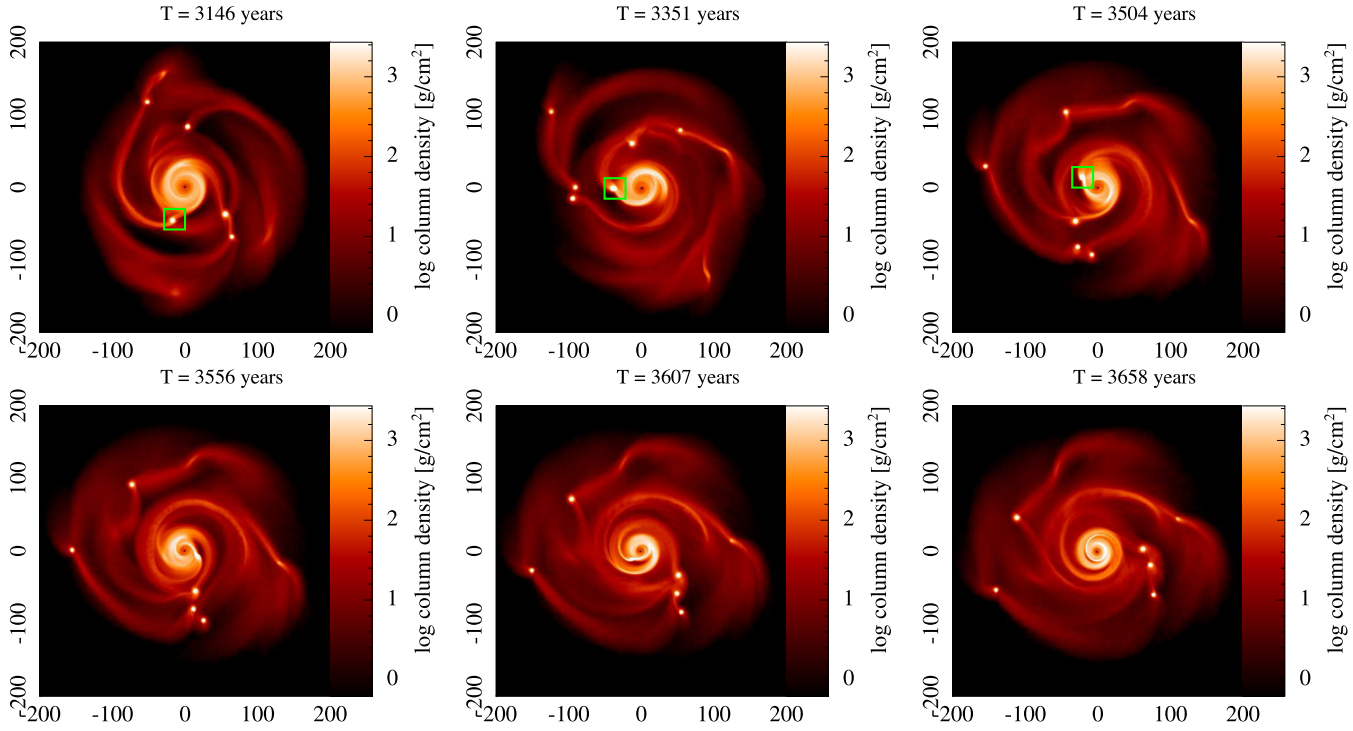

Figure 22. Column density plots of simulation 7, increasing in time, showing the tidal disruption of clump 4, marked in green in the top three images before it begins to be tidally destroyed.

cores, a key assumption in the core-assisted gas-capture hypothesis (CAGC) of Nayakshin, Helled & Boley (2014).

In addition to encounters scattering fragments out to large radii, we also find a tentative relationship between the dominant azimuthal wavenumber in the disc, and the maximum semimajor axis of a clump in that disc, such that $a_{\max} \propto 1/m$. This seems to suggest that the spiral arms of protoplanetary discs play as large a role in the dynamical fate of the clumps as do the clump–clump scatterings. Although this relationship is preliminary, and requires more simulations in a range of disc-to-star mass ratios to confirm it [since $m \sim 1/q$ (Dong et al. 2015), where q is disc-to-star mass ratio], it is unsurprising that such a relationship may exist, and we suspect that the relationship is one of inverse proportionality, rather than one of negative proportionality, due to the relationship between gravitational torque Γ_G and azimuthal wavenumber as follows (for a full derivation and comprehensive explanation, we refer the reader to Binney & Tremaine 2008). The gravitational torque Γ_G exerted on material outside a radius R_0 in a disc is given by

$$\Gamma_G = \mathrm{sgn}(k)\frac{\pi^2 m R_0 G \Sigma_1^2}{k^2}, \tag{17}$$

where Σ_1 is a gentle function of radius, k is the radial wavenumber defined as

$$k \equiv \frac{\partial(mf(R))}{\partial R}, \tag{18}$$

$mf(R)$ is the radial shape function of the spiral (for a simple example, see Hall et al. 2016), and $\mathrm{sgn}(k) = +1$ for trailing spirals (i.e. positive torque exerted outwards). At a given value of R_0, and the same function for Σ_1, we can see that

$$\Gamma_G \propto \frac{1}{m}. \tag{19}$$

To establish the relationship $a_{\max} \propto 1/m$, we have assumed that the amount of torque is directly proportional to the change in radial distance. Whilst this is almost certainly an oversimplification of

matters, we can see from

$$\Gamma_{\rm G} = \frac{{\rm d}|\vec{L}|}{{\rm d}t} = \frac{\rm d}{{\rm d}t}(m|\vec{v}\times\vec{r}|) = \frac{\rm d}{{\rm d}t}(m|\vec{v}||\vec{r}|\sin[\theta]), \quad (20)$$

that if we assume mass, velocity, and the angle between $\vec{v}$ and $\vec{r}$ stay fairly constant, then $\Gamma_{\rm G} \propto {\rm d}r/{\rm d}t$, i.e. the distance we wish to move our fragment. Assuming that all fragments form at roughly the same r in a given disc, (i.e. where that particular disc becomes susceptible to fragmentation), then we recover $a_{\rm max} \propto 1/m$.

Varying the surface density profile in a protostellar disc will alter disc torques and migration rates of planets (see e.g. Baruteau, Meru & Paardekooper 2011). Since we simulated nine protostellar discs that had initially identical surface density profiles, this is not something we have investigated, but it could potentially alter our results. For example, steeper surface density profiles correspond to more rapid migration rates. It is therefore feasible that a sharp cut-off at the disc outer edge, as we use in our initial conditions, may exacerbate migration torques in the disc. However, since the majority of the disc mass is contained well within the disc's numerical outer edge, it is probably reasonable to assume it is not the dominant effect when considering the radial migration of fragments.

Despite the relatively short time-scales of our simulations (since we did not make use of sink particles), we can see that orbital properties of fragments are drastically altered by interactions with each other. Since disc fragmentation forms objects with initially low eccentricities ($e < 0.1$), it is generally accepted that measurements of eccentricity as a function of orbital distance will constrain the formation mechanism of giant planets and brown dwarfs (Vorobyov 2013), with high eccentricity being caused by dynamical scattering.

However, our results in Fig. 12 possibly suggest that these high eccentricity orbits could be formed at very early times, during the gas phase of the disc, and as such eccentricity measurements of brown dwarfs and giant planets may not, necessarily, constrain their formation mechanism. We have shown that the initial orbital inclination of our fragments is reduced by a factor of $\sim$100 over the duration of the simulation (Fig. 13), despite the significant dynamical interactions many of the fragments experience. This suggests that although dynamical interactions certainly can create highly inclined orbits, doing so while the gas disc is present may be much more difficult.

On the other hand, our simulations are of discs in isolation. Inclination and eccentricity may be excited by environment, such as a stellar companion, or location within a cluster environment (Forgan et al. 2015). Since current GIPS models do not include eccentricity or inclination information, we have provided several Gaussian fits in Fig. 13 from our SPH simulation data. Despite our small sample size, we hope these plots will be useful in further development of GIPS models.

In this work, we do not consider how solid particles will effect the formation, evolution and survival of the clumps, nor their effects on the behaviour of the gas. This is, quite possibly, the most important limitation of our work. As we have already discussed, opacity could heavily influence the initial mass distribution of our clumps. It is also feasible that altering the opacity in the clumps, due to movement of solids, could result in clumps cooling more (or less) rapidly, resulting in more (or fewer) clumps surviving (Nayakshin 2010). More clumps surviving because of local opacity changes could present a partial solution to the rapid inward migration and subsequent disruption of GI fragments found in so many other works (see e.g. Vorobyov & Basu 2005; Baruteau et al. 2011; Zhu et al. 2012).

To date, no global 3D SPH simulations of dusty, self-gravitating, fragmenting protostellar discs have been conducted. This is a computationally expensive task, with complicated physics. Almost certainly, a full treatment of radiation hydrodynamics would be necessary to correctly capture the cooling of the system, and the spatial evolution of the dust within the gas. High resolution is needed in the core of these fragments to trace their compositional change. However, if we are considering the global evolution of the system, we must be able to capture the full dynamical range. This is probably not possible with current computational abilities, and is one of many multiphysics problems present in protostellar disc modelling (Haworth et al. 2016).

How fragmentation proceeds when solid grains are included in the simulation is clearly an interesting question. Although not considered in 3D hydrodynamics simulations, this idea has recently been explored by Nayakshin et al. (2014), in their so-called CAGC paradigm. In this scenario, grain sedimentation inside a fragment forms a core of heavy elements. Upon reaching a critical core mass, the surrounding gaseous envelope collapses on to the core, analogous to the core accretion paradigm. The assumption in the work of CAGC is, of course, that these cores *do* form. GI tends to occur beyond $\sim$50 au in protostellar discs (Rafikov 2005). For a significant core to form in GI clumps due to grain sedimentation, there must be a substantial local dust-to-gas ratio at the site of clump formation. Since dust grains tend to migrate rapidly inwards (Weidenschilling 1977), it may well be difficult to maintain a significant dust-to-gas ratio at the site of fragmentation, making core formation from grain sedimentation inside a fragment difficult. However, GI is also a rapid process, so as long as the fragmentation takes place rapidly, then the local change in pressure gradient may be sufficient to prevent inward migration of these grains.

If massive cores in GI clumps *do* form, as assumed by CAGC, then we should probably expect differences in the final clump distributions to what we have presented here. An interesting feature of the (CAGC) paradigm is that if planets are formed by this method, then we should expect a positive metallicity correlation.

Assuming, for now, that the collapse proceeds with no core mediation, then it is probably reasonable to expect no metallicity correlation; indeed, there is at least *some* numerical evidence that we may expect a *negative* metallicity correlation (Cai et al. 2005), since low metallicity corresponds to faster cooling (and therefore stronger spiral amplitudes, increasing the effective gravitational stress) which may result in fragmentation. This is because higher metallicity results in better cooling only in the optically thin regime, for example, at the tenuous surface of the disc.

Conversely, higher metallicity results in slower cooling in the optically thick regime, i.e. at the disc mid-plane, which is the location of fragmentation. Therefore, gas giant planets formed through GI should be preferentially found around *low*-metallicity stars. It seems to now be fairly clear that GI rarely forms planetary mass objects (Rice et al. 2015), but if it does, these objects will be much larger than Jupiter. We should, then, find that planets more massive than Jupiter are more frequent around low-metal stars. However, it has been suggested that this is not the case, since planets more massive than $\sim$3 M_J seem to be found *less* often around low-metallicity stars (Thorngren et al. 2016).

Overall, the picture is unclear. While CAGC may result in a positive metallicity correlation, there seems to be enough evidence

to suggest that fragmentation should preferentially occur in discs around low-metallicity stars, which, in turn, suggests that GI planets would be preferentially found around low-metallicity stars. In the CAGC paradigm, fragmentation must first take place, before the core can form through subsequent grain sedimentation. If this fragmentation happens less often around high-metallicity stars, this could still result in an over negative metallicity correlation. Ultimately, the ambiguity of what happens at low metallicity does not remove the strong high-metallicity correlation with planet frequency. This is mostly suspected to be the work of core accretion, and is difficult to explain with any GI theory alone.

The work we have presented here outlines the first direct comparison between a GIPS model and a suite of 3D, global hydrodynamics simulations of fragmenting protostellar discs. While the work of Forgan & Rice (2013) presents the first attempt at a GIPS model, it is not the only one (see e.g. Galvagni & Mayer 2014; Nayakshin & Fletcher 2015, and a recent extension to the Forgan & Rice 2013 model in Forgan et al. 2015). As mentioned in the introduction to this work, our simulations are run for as long as is computationally feasible without the use of sink particles, since part of our aim was to characterize the internal density and temperature profile of these fragments. However, doing so limits us to very early times in the disc, typically around ∼4000 years or so after the disc has initially formed. For this reason, we did not compare our results to the models of Forgan et al. (2015), which consider the ultimate dynamical fate of the fragments after disc dispersal.

Similarly, the work of Forgan & Rice (2013) considers the fragmentation phase of a disc, unlike Galvagni & Mayer (2014). Since our hydrodynamical simulations are analysed around the fragmentation phase, we wished to use a model that did not assume already that clumps exist in the disc, ruling out the Galvagni & Mayer (2014) models. Finally, we considered the Nayakshin & Fletcher (2015) models unsuitable for direct comparison to our hydrodynamics simulations because only one fragment per disc is simulated, unlike the population synthesis models of Forgan & Rice (2013), which places multiple fragments in a disc susceptible to fragmentation at separations of a few Hill radii. We stress here that we are not suggesting the superiority of the Forgan & Rice (2013) models, simply that those particular models were best suited for direct comparison to our hydrodynamics simulations.

Of the 41 clumps that are detected in these simulations, seven were tidally destroyed (∼20 per cent), and two have orbits with eccentricity approaching unity ($e \sim 0.75$), which suggests that they are on their way to being ejected (∼5 per cent). If these clumps *are* ultimately ejected, then GI could, perhaps, also contribute to the population of free-floating planets (Rice et al. 2003b; Forgan et al. 2015). We have demonstrated that the orbital and structural evolution of neighbouring fragments are linked; we recommend therefore that any future population synthesis models are able to account for this.

ACKNOWLEDGEMENTS

We thank the anonymous referee for their constructive comments, which greatly improved the discussion in this paper. We would like to thank Daniel Price for his publicly available SPH plotting code SPLASH (Price 2007), which we used to produce Figs 1, 15, 21 and 22. We also thank Fabian Fischer for his online LaTex Overlay Generator (available here: https://ff.cx/latex-overlay/), which we used to annotate Figs 15, 21 and 22. KR gratefully acknowledges support from STFC grant ST/M001229/1. DF gratefully acknowledges support from the ECOGAL project, grant agreement 291227, funded by the European Research Council under ERC-2011-ADG. The research leading to these results also received funding from the European Union Seventh Framework Programme (FP7/2007-2013) under grant agreement number 313014 (ETAEARTH). This project has received funding from the European Research Council (ERC) under the European Union's Horizon 2020 research and innovation programme (grant agreement No. 681601).

REFERENCES

Barnes J. E., Hut P., 1989, ApJS, 70, 389
Baruteau C., Meru F., Paardekooper S.-J., 2011, MNRAS, 416, 1971
Bate M. R., 2005, MNRAS, 363, 363
Bate M. R., Bonnell I. A., Price N. M., 1995, MNRAS, 277, 362
Binney J., Tremaine S., 2008, Galactic Dynamics, 2nd edn. Princeton Univ. Press, Princeton, NJ
Bodenheimer P., Yorke H. W., Rozyczka M., Tohline J. E., 1990, ApJ, 355, 651
Boley A. C., Hayfield T., Mayer L., Durisen R. H., 2010, Icarus, 207, 509
Boley A. C., Helled R., Payne M. J., 2011, ApJ, 735, 30
Boss A. P., 1997, Science, 276, 1836
Boss A. P., 1998, ApJ, 503, 923
Boss A. P., 2002, ApJ, 567, L149
Cai K., Durisen R. H., Michael S., Boley A. C., Mejía A. C., Pickett M. K., D'Alessio P., 2005, in Protostars and Planets V Posters. p. 8155
Cameron A. G. W., 1978, Moon Planets, 18, 5
Cleary P. W., Monaghan J. J., 1999, JCAP, 148, 227
D'Angelo G., Lubow S. H., 2010, ApJ, 724, 730
Dong R., Hall C., Rice K., Chiang E., 2015, ApJ, 812, L32
Fang J., Margot J.-L., 2013, ApJ, 767, 115
Figueira P. et al., 2012, A&A, 541, A139
Fischer D. A., Valenti J., 2005, ApJ, 622, 1102
Forgan D., Rice K., 2011, MNRAS, 417, 1928
Forgan D., Rice K., 2013, MNRAS, 432, 3168
Forgan D., Rice K., Stamatellos D., Whitworth A., 2009, MNRAS, 394, 882
Forgan D., Parker R. J., Rice K., 2015, MNRAS, 447, 836
Forgan D., Price D. J., Bonnel I., 2016, submitted
Galvagni M., Mayer L., 2014, MNRAS, 437, 2909
Gingold R. A., Monaghan J. J., 1977, MNRAS, 181, 375
Haisch K. E., Jr, Lada E. A., Lada C. J., 2001, ApJ, 553, L153
Hall C., Forgan D., Rice K., Harries T. J., Klaassen P. D., Biller B., 2016, MNRAS, 458, 306
Haworth T. J. et al., 2016, PASA, 33, e053
Hubickyj O., Bodenheimer P., Lissauer J. J., 2005, Icarus, 179, 415
Kley W., Nelson R. P., 2012, ARA&A, 50, 211
Kratter K. M., Murray-Clay R. A., Youdin A. N., 2010, ApJ, 710, 1375
Kuiper G. P., 1951, Proc. Natl. Acad. Sci., 37, 1
Lambrechts M., Johansen A., 2012, A&A, 544, A32
Levison H. F., Kretke K. A., Duncan M. J., 2015, Nature, 524, 322
Li Y., Kouwenhoven M. B. N., Stamatellos D., Goodwin S. P., 2016, ApJ, 831, 166
Lissauer J. J., 1993, ARA&A, 31, 129
Lodato G., Rice W. K. M., 2004, MNRAS, 351, 630
Lodato G., Rice W. K. M., 2005, MNRAS, 358, 1489
Lucy L. B., 1977, AJ, 82, 1013
Marois C., Macintosh B., Barman T., Zuckerman B., Song I., Patience J., Lafrenière D., Doyon R., 2008, Science, 322, 1348
Marois C., Zuckerman B., Konopacky Q. M., Macintosh B., Barman T., 2010, Nature, 468, 1080
Masunaga H., Inutsuka S.-i., 1999, ApJ, 510, 822
Masunaga H., Miyama S. M., Inutsuka S.-i., 1998, ApJ, 495, 346
Mayer L., Lufkin G., Quinn T., Wadsley J., 2007, ApJ, 661, L77
Monaghan J. J., 1992, ARA&A, 30, 543
Monaghan J. J., 2005, Rep. Prog. Phys., 68, 1703
Naoz S., Farr W. M., Lithwick Y., Rasio F. A., Teyssandier J., 2013, MNRAS, 431, 2155
Nayakshin S., 2010, MNRAS, 408, L36

Nayakshin S., 2011a, MNRAS, 413, 1462
Nayakshin S., 2011b, MNRAS, 416, 2974
Nayakshin S., Fletcher M., 2015, MNRAS, 452, 1654
Nayakshin S., Lodato G., 2012, MNRAS, 426, 70
Nayakshin S., Helled R., Boley A. C., 2014, MNRAS, 440, 3797
Nero D., Bjorkman J. E., 2009, ApJ, 702, L163
Pollack J. B., Hubickyj O., Bodenheimer P., Lissauer J. J., Podolak M., Greenzweig Y., 1996, Icarus, 124, 62
Price D. J., 2007, PASA, 24, 159
Rafikov R. R., 2005, ApJ, 621, L69
Rice W. K. M., Armitage P. J., 2009, MNRAS, 396, 2228
Rice W. K. M., Armitage P. J., Bate M. R., Bonnell I. A., 2003a, MNRAS, 339, 1025
Rice W. K. M., Armitage P. J., Bonnell I. A., Bate M. R., Jeffers S. V., Vine S. G., 2003b, MNRAS, 346, L36
Rice K., Lopez E., Forgan D., Biller B., 2015, MNRAS, 454, 1940
Rosswog S., 2009, New Astron. Rev., 53, 78
Santos N. C., Israelian G., Mayor M., 2004, A&A, 415, 1153
Semenov D., Henning T., Helling C., Ilgner M., Sedlmayr E., 2003, A&A, 410, 611
Smith R. J., Clark P. C., Bonnell I. A., 2008, MNRAS, 391, 1091
Springel V., White S. D. M., Tormen G., Kauffmann G., 2001, MNRAS, 328, 726
Srisawat C. et al., 2013, MNRAS, 436, 150
Stamatellos D., 2015, ApJ, 810, L11
Stamatellos D., Whitworth A. P., 2005, A&A, 439, 153
Stamatellos D., Whitworth A. P., 2009, MNRAS, 400, 1563
Stamatellos D., Whitworth A. P., Bisbas T., Goodwin S., 2007, A&A, 475, 37
Thorngren D. P., Fortney J. J., Murray-Clay R. A., Lopez E. D., 2016, ApJ, 831, 64
Tobin J. J. et al., 2016, Nature, 538, 483
Vorobyov E. I., 2013, A&A, 552, A129
Vorobyov E. I., Basu S., 2005, ApJ, 633, L137
Vorobyov E. I., Zakhozhay O. V., Dunham M. M., 2013, MNRAS, 433, 3256
Weidenschilling S. J., 1977, MNRAS, 180, 57
Wilkins D. R., Clarke C. J., 2012, MNRAS, 419, 3368
Williams J. P., de Geus E. J., Blitz L., 1994, ApJ, 428, 693
Windmark F., Birnstiel T., Güttler C., Blum J., Dullemond C. P., Henning T., 2012, A&A, 540, A73
Youdin A. N., 2011, ApJ, 731, 99
Youdin A. N., Goodman J., 2005, ApJ, 620, 459
Zhu Z., Hartmann L., Nelson R. P., Gammie C. F., 2012, ApJ, 746, 110

This paper has been typeset from a TEX/LATEX file prepared by the author.